



# Ocean Circulation from Space

Rosemary Morrow<sup>1</sup> · Lee-Lueng Fu<sup>2</sup> · Marie-Hélène Rio<sup>3</sup> · Richard Ray<sup>4</sup> · Pierre Prandi<sup>5</sup> · Pierre-Yves Le Traon<sup>6</sup> · Jérôme Benveniste<sup>3</sup>

Received: 10 November 2022 / Accepted: 15 February 2023 / Published online: 30 March 2023  
© The Author(s) 2023

## Abstract

This paper reviews the recent progress in our estimation of ocean dynamic topography and the derived surface geostrophic currents, mainly based on multiple nadir radar altimeter missions. These altimetric observations provide the cornerstone of our ocean circulation observing system from space. The largest signal in sea surface topography is from the mean surface dominated by the marine geoid, and we will discuss recent progress in observing the mean ocean circulation from altimetry, once the geoid and other corrections have been estimated and removed. We then address the recent advances in our observations of the large-scale and mesoscale ocean circulation from space, and the particular challenges and opportunities for new observations in the polar regions. The active research in the ocean barotropic tides and internal tidal circulation is also presented. The paper also addresses how our networks of global multi-satellite and in situ observations are being combined and assimilated to characterize the four-dimensional ocean circulation, for climate research and ocean forecasting systems. For the future of ocean circulation from space, the need for continuity of our current observing system is crucial, and we discuss the exciting enhancement to come with global wide-swath altimetry, the extension into the coastal and high-latitude regions, and proposals for direct total surface current satellites in the 2030 period.

**Keywords** Satellite oceanography · Ocean circulation · Mesoscale · Tides · Polar oceans · Ocean forecasting

## List of Acronyms

ADT Absolute Dynamic Topography: ocean topography including the mean and time-variable components

---

✉ Rosemary Morrow  
Rosemary.Morrow@legos.obs-mip.fr

<sup>1</sup> LEGOS/University Toulouse III, 14 Avenue Edouard Belin, 31400 Toulouse, France

<sup>2</sup> Jet Propulsion Laboratory, California Institute of Technology, 4800 Oak Grove Dr, Pasadena, CA 91109, USA

<sup>3</sup> European Space Agency, ESRIN, Largo Galileo Galilei 1, 00044 Frascati, Italy

<sup>4</sup> NASA Goddard Space Flight Center, Mailcode 130, Greenbelt, MD 20781, USA

<sup>5</sup> CLS Group, 11 Rue Hermes, 31520 Ramonville-St-Agne, France

<sup>6</sup> Mercator-Ocean International, 2 Avenue de L'Aerodrome de Montaudran, 31400 Toulouse, France

Argo	An international program of profiling floats to observe ocean temperature, salinity, currents
AVISO & AVISO+BRAT	CNES altimetry data portal Broadview Radar Altimetry Tutorial and Toolbox (BRAT) is an online altimetry tutorial from ESA & CNES
CHAMP	Challenging Minisatellite Payload (CHAMP) was a German satellite launched in 2000 to study the Earth's gravity field
CLIVAR	The international Climate Variability Program, part of the WCRP.
CLS	Collecte Location Satellite
CMEMS	European Union's Copernicus Marine Environment Monitoring Service (CMEMS), implemented and operated by Mercator Ocean, provides oceanographic products and services
CNES	Centre Nationale d'Etudes Spatiales: French Space Agency
Copernicus	Previously known as GMES (Global Monitoring for Environment and Security), is the European Union's Earth observation program
CRISTAL	Copernicus Polar Ice and Snow Topography Altimeter mission from ESA for the cryosphere
CryoSat & CryoSat-2	ESA satellite altimeters dedicated to polar observation.
CSA	Canadian Space Agency
CTD	Conductivity Temperature Depth sensors
DUACS	Operationnal multimission production system of altimeter data developed by CNES/CLS
EKE	Eddy kinetic energy
ENSO	El Nino Southern Oscillation climate mode
ERS	European Remote Sensing satellite was the European Space Agency's first Earth-observing satellite programme using a polar orbit
ESA	European Space Agency
EUMETSAT	European operational satellite agency for monitoring weather, climate and the environment from space
GEOS-3	Geodynamics Experimental Ocean Satellite 3, was the third and final satellite as part of NASA's Geodetic Earth Orbiting Satellite/Geodynamics Experimental Ocean Satellite program in 1975–1979
Geosat	GEOdetic SATellite was a U.S. Navy radar altimeter satellite, 1985–1989
Geosat-FO	Geosat-Follow-On. US Navy/NOAA radar altimeter satellite, 1998–2008
GOCE	Gravity Field and Steady-State Ocean Circulation Explorer) was the first of ESA's Living Planet Programme satellites to map the Earth's gravity field
GRACE	The Gravity Recovery and Climate Experiment (GRACE) was a joint mission of NASA and the German Aerospace Center (DLR). Twin satellites took detailed measurements of Earth's gravity field anomalies
HARMONY	A proposed ESA Earth Explorer mission, with a constellation of two SAR satellites to fly in tandem with Sentinel-1 after 2029
HY-2	Haiyang (HY, Chinese; pinyin: Hǎiyáng; lit. 'ocean') is a series of marine remote sensing satellites developed and operated by the People's Republic of China since 2002

ISRO	Indian Space Research Organisation is the Indian Space Agency
Jason	Jason-1, Jason-2, Jason-3 are NASA/CNES/NOAA/Eumetsat precise radar altimeters, following on from Topex/Poseidon
JPL	Jet Propulsion Laboratory
KaRIn	Ka-band radar Interferometry wide-swath altimeter instrument on SWOT
LEGOS	Laboratoire des Etudes en Géophysique et Océanographie Spatiale, French research laboratory in Toulouse
LRM	Low Resolution Mode
MDT	Mean Dynamic Topography. Time-mean component of the ocean's dynamical topography, not including the marine geoid
MOSAiC	Multidisciplinary drifting Observatory for the Study of Arctic Climate
MSS	Mean Sea Surface. Time-mean component of the ocean topography including the marine geoid
NASA	National Aeronautics and Space Administration: US civil Space Agency
NOAA	US National Oceanic and Atmospheric Administration agency for monitoring weather, climate and the environment
NSOAS	Chinese National Satellite Ocean Application Service
OdYSEA	Proposed NASA/CNES Doppler scatterometry mission for global-scale surface currents along with surface-level scatterometer winds
OSTST	Ocean Surface Topography Science Team: International Team of scientists and engineers specializing in radar altimetry for oceans and Earth Observation
PDO	Pacific Decadal Oscillation climate mode
SAR	Synthetic Aperture Radar
SAR-In	Synthetic Aperture Radar Interferometry
Saral/AltiKa	CNES/ISRO radar altimeter in Ka-band frequency
SeaSat	Sea Satellite: NASA/JPL satellite dedicated to oceanographic applications in 1978
Sentinel-3, -6	Earth observation satellite series developed by ESA as part of the Copernicus Program
Skylab	First US space station launched by NASA, 1973-1974
SSH	Sea Surface Height
SWOT	Surface Water Ocean Topography SARIn wide-swath altimeter
T/P	Topex/Poseidon: NASA/CNES precise radar altimeter satellite
UKSA	United Kingdom Space Agency
WRCP	World Climate Research Program is an international program that helps to coordinate global climate research
XBT	EXpendable BathyThermograph ocean temperature profiles

## Article Highlights

- Reviews recent progress in estimating ocean dynamic topography and derived geostrophic currents at large and mesoscales from radar altimeter missions

- Reviews advances in estimating ocean barotropic tides and internal tides, the marine geoid and mean circulation, and polar ocean circulation
- Reviews advances in characterizing the 4D ocean circulation, for climate research and ocean forecasting systems

## 1 Introduction

The oceans are a major reservoir of heat, freshwater, salt, nutrients and carbon in the Earth system. On a global scale, the ocean has absorbed more than 90% of the excess of heat from global warming since the industrial revolution (Levitus et al. 2009). Heat, salt, nutrients, carbon and freshwater are redistributed across ocean basins and exchanged vertically by ocean currents: the ocean circulation. The ocean circulation varies on a wide range of space and time scales: It includes the small-scale mixing and rapid movements due to waves and tides, to the energetic adjustment from mesoscale eddies and fronts, up to the large-scale currents and gyre circulation and the interannual to decadal variations from climate modes (Fu and Chelton 2001). Global observations of this wide range of space and time-scales of the ocean circulation remain very challenging.

The development of satellite remote sensing of the global ocean circulation began in the 1970s (Fu et al. 2019). This allowed a transition from observing the ocean from an in situ perspective, based on slow, shipborne efforts or moorings, to remote sensing which allowed us to sample the global ocean in a relatively short period of time. One critical point in remote sensing over the oceans is that most of the electromagnetic radiation does not propagate through water. Therefore, all satellite observations measure the surface, or near-surface ocean properties: surface tracers (temperature, salinity, ocean color) or surface fronts and slicks, surface winds or the sea surface topography. Even though sea surface topography observed by satellite radar altimeter is a surface variable, its value reflects the depth-integrated variations of density and pressure in the ocean. When combined with knowledge of the ocean vertical structure, from theory or from ocean observations or models, satellite altimetry becomes a powerful tool to observe not just the surface topography and the derived surface geostrophic currents, but also the depth-integrated ocean circulation.

Before the 1960s when modern electronics enabled the collection of longtime series of ocean currents from moorings or underway observations of temperature and salinity, the notion of large-scale ocean circulation was that of a stable fluid. The discovery of the rapidly changing and meandering currents associated with oceanic mesoscale eddies called for the need to map ocean currents with better spatial and temporal resolution. The first global map of the variability of the sea surface height (SSH) derived from only one month of satellite altimetry data from Seasat was a revelation (Cheney et al. 1983).

This paper on Ocean Circulation from Space will review the progress in our estimation of ocean dynamic topography and the derived geostrophic currents, mainly based on nadir radar altimeter missions. These operate in the conventional “low-resolution” mode (LRM), described in Sect. 2, and the more recent, more precise and higher resolution Synthetic Aperture Radar (SAR) nadir mode, described in Sect. 3. These altimetric observations provide the cornerstone of our ocean circulation observing system from space. The data can be used at their highest resolution along their tracks (e.g., for fine-scale analyses or in data assimilation), or are re-gridded into multi-mission maps of altimetric surface height and geostrophic currents, incorporating data from all altimetry missions to increase the

space–time sampling. These maps are widely used by the ocean community to observe the ocean circulation at scales  $> 100$ – $200$  km in wavelength.

As ocean models are improving their estimation of finer-scale ocean circulation, there is a need for finer-scale observations to validate them. A new generation of altimeters is starting to use wide-swath SAR-interferometry (SAR-In) modes. The first global wide-swath SAR-In mission is planned with the NASA-CNES SWOT mission (launched in December 2022; Fu and Rodriguez 2004; Morrow et al. 2019); a future Chinese Guanlan mission (Chen et al. 2019) is also planned. Section 4 will include a description of these recent technological advances, and how the new observations with improved spatial resolution and lower noise will allow us to observe the finer-scale ocean circulation.

When measuring sea surface topography from space, the largest signal is that of the marine geoid, which is quasi-stationary in time compared to the more rapid sea surface topography changes due to the ocean circulation variations. Observing the Earth's gravity field and its variations from space is critical for monitoring the ever-changing mass of water on Earth with applications to oceanography, hydrology, and geodesy. The large-scale Earth gravity field and marine geoid can be determined from specific gravity missions, such as NASA's GRACE mission or ESA's GOCE mission. Satellite radar altimetry also provides an excellent global observation of the fine-scale marine geoid and its slope beneath the ground tracks, since the sea surface is also a surface of constant gravitational potential (Sandwell and Smith 2009). Whether at large or smaller scale, the marine geoid is not in geostrophic balance, and needs to be removed from radar altimetry measurements of the sea surface height for ocean circulation studies. For exactly repeating altimeter tracks, the geoid and its uncertainties can be removed by subtracting the mean signal from the alongtrack altimetric sea surface height. For non-repeat altimeter tracks, or missions on a new repeating orbit, an independent gridded estimate of the marine geoid is required, based on a combination of satellite Earth gravity missions, all altimetric missions, and in situ gravity observations. In Sect. 5, we discuss the recent progress in understanding the mean ocean circulation, which is closely linked to our ability to estimate and remove an accurate marine geoid.

Once the geoid and other corrections have been removed, the ocean circulation can be derived from the altimetric sea surface height under the approximation of geostrophic balance. This generally covers the most energetic adjustment processes of the ocean mesoscale (20–250 km) eddies and meanders, the large-scale ocean planetary waves (Rossby waves, Kelvin waves, etc.), up to the larger-scale ocean circulation of the gyres and boundary currents. The contributions of satellite altimetry to our understanding of the large-scale and mesoscale processes will be discussed in Sects. 6 and 7.

Due to their large amplitude signals and short scales, the energetic oceanic mesoscale eddies were the first features of ocean circulation detected by satellite observations. Over the last few decades, great progress has been made in estimating the larger mesoscale dynamics from satellite altimetry, with scales  $> 200$  km in wavelength (see Sect. 7). At larger scales, the variability and mean state of the ocean circulation are more difficult to observe from space (see Sect. 6). Large-scale errors in the satellite's orbit, or in the tidal estimates or other corrections to the radar range measurements, can mask the cm-level signals of the large-scale ocean circulation. Determining the large-scale SSH change requires a high precision of the altimetric measurement and corrections at a cm level that has taken a long period of time to develop. Yet the advancement of satellite altimetry from the 1970s to the present has been a crucial factor in improving our knowledge of the global ocean circulation from the mesoscale to the basin-scale and has revolutionized the field of physical oceanography.

There are specific challenges in our ability to observe the ocean circulation at higher latitudes in the polar seas. This is related to the presence of sea ice that blocks the observation of the ocean surface, and causes strong backscattering of the radar signal, even in the open leads or polynyas. Although the ground tracks converge at higher latitudes with better spatial–temporal coverage, there are fewer valid altimetric observations and fewer missions (the Jason series reaches only  $66^\circ$  in latitude). The polar orbiting missions provide the best opportunity for high-latitude ocean circulation studies, but some are Sun-synchronous, meaning more uncertainties in their tidal estimates here. Recent advances have improved our estimate of the altimetric sea surface height in the Polar Regions, and the derived ocean circulation, which will be described in Sect. 8.

Ocean tides and internal tides have distinct sea surface height signals that are well detected in radar altimetry. The different repeat cycles of altimetric missions alias the diurnal and semi-diurnal tidal constituents into lower frequencies. This was recognized in early altimetric studies, and the choice of altimetric orbit can be specifically designed to separate the main tidal constituents after a number of years of operation. Non Sun-synchronous orbits are generally better in resolving the major ocean tides, and the Topex–Poseidon–Jason series has provided a fundamental advance in our estimation of global ocean barotropic tides (Ray and Egbert 2017). Internal tides in a stratified ocean have a smaller signal (few cm) and their coherent, phase-locked components have been well observed with alongtrack satellite altimetry (Ray and Zaron 2016). The strong interaction between the internal tide and the ocean circulation generating incoherent or non-phase-locked internal tides has been recently revealed in ocean models and altimetric observations (Zaron 2017; Richman et al. 2012; Tchilibou et al. 2018). This is a challenge for ocean circulation studies, since accurate geostrophic currents require a good separation of the unbalanced internal tide from the sea surface height observation. Many studies are working on innovative techniques to address this challenge. Satellite altimetry, from nadir to wide-swath observations, provide an excellent opportunity to observe the interaction of the internal tide with unstable currents, one of the uncharted pathways to smaller scale mixing and dissipation. This active domain of satellite observation and studies will be described in Sect. 9.

Highly complementary to radar altimetry observations was the development of the global international in situ Argo Program (Roemmich et al. 2009). Beginning in the early 2000s, Argo has evolved into an international program that has deployed nearly 4000 floats in the global ocean sampling the temperature and salinity of the upper 2000 m of the water column. This global measurement is complementary to the ship-based observations from conductivity, temperature and depth sensors (CTDs) or expendable bathythermograph (XBT) instruments, mooring data, and the global surface drifter observations. These regular in situ measurements, coupled with ocean surface topography from altimetry, have provided essential information on the geostrophic circulation of the world's oceans, as well as the density field of the ocean. Ocean observing satellites, together with in situ ocean observing platforms such as from Argo, and observationally constrained ocean state estimation systems, are providing quantitative characterization of the four-dimensional ocean circulation. These advances in the domain of altimetric assimilation and ocean reanalyses will be addressed in Sect. 10. By better observing the 4D Ocean circulation, we have an improved understanding of its role on climate and weather processes, its linkages with the global water cycle, and its impacts on ocean biogeochemistry. These observations are also playing a pivotal role in improving climate and weather predictions.

## 2 Conventional Radar Altimetry Observations of Ocean Circulation

In the open ocean away from the equator, the slow-moving state of the large-scale ocean circulation is in geostrophic balance; the Coriolis force exerted on the moving fluid is balanced by the horizontal pressure gradient as shown by the following equations:

$$fv = \frac{1}{\rho} \frac{\partial p}{\partial x} \quad (1)$$

$$fu = -\frac{1}{\rho} \frac{\partial p}{\partial y} \quad (2)$$

$$0 = -\frac{\partial \rho}{\partial z} - g\rho \quad (3)$$

where  $p$  is the pressure,  $\rho$  is the density of seawater,  $g$  is the Earth's gravity acceleration,  $u$  and  $v$  are the zonal and meridional velocity components, respectively,  $f$  is the Coriolis parameter defined as  $f=2\Omega \sin \varphi$ , where  $\Omega$  is the Earth's rotation rate ( $7.292 \times 10^{-5}$  rad/sec), and  $\varphi$  is the latitude. These equations for hydrostatic and geostrophic balance allow the computation of the velocity at the surface relative to a deep level from the horizontal gradient of the ocean's density field as follows:

$$\rho v = -\frac{g}{f} \int_{z_o}^z \frac{\partial \rho}{\partial x} dz + v_o \quad (4)$$

where  $z_o$  is a reference level for the integration and  $v_o$  is the meridional velocity at the reference level. A similar equation can be obtained for  $u$ . This method based on the "thermal wind" equation has been the main approach used to determine ocean general circulation from shipboard measurements of the ocean density field (see Wunsch and Ferrari 2018). However, the determination of the velocity at the reference level has been an elusive goal. The idea of making measurements of the height of sea surface from space after subtracting an independent estimate of the geoid and tides to determine the surface ocean general circulation was part of the original rationale for developing satellite altimetry and gravimetry. Once the surface geostrophic velocity is known at  $z = 0$ , then the geostrophic velocity at deep levels can be determined from (Eq. 4).

The first satellite radar altimetry missions to observe the sea surface topography and derived geostrophic currents were launched in the 1970s (Skylab in 1973, then GEOS-3 from 1975–1979) followed by Seasat in 1978, which carried a radar altimeter, a scatterometer, and a synthetic aperture radar (SAR). These early missions demonstrated that global ocean circulation could be monitored from space, although with large errors in their orbit estimation and different corrections, with a sea surface height (SSH) accuracy of around 1 m, but this was primarily orbit error for Seasat, which could be minimized for mapping mesoscale features. In the late 1980s, the Geosat mission (US Navy, 1985–1990) flew with an 18-month geodetic phase to improve the Earth's gravity and marine geoid estimates, followed by a 3-year ocean circulation phase. With unique post-processing of both Seasat and Geosat data, Leben et al. (2011) successfully mapped large-scale Pacific Ocean sea surface height differences between 1978 (Seasat) and 1987 (Geosat).

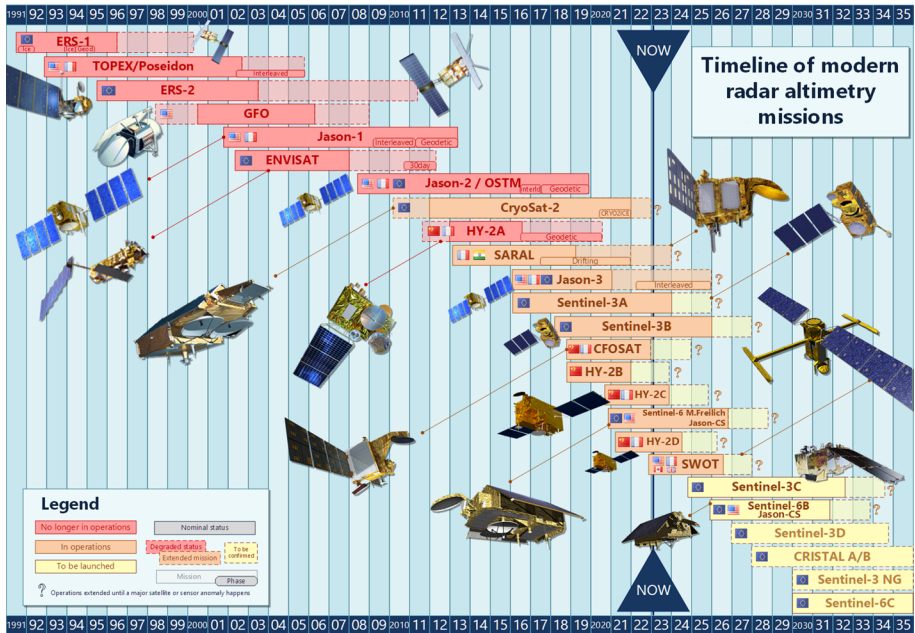


**Fig. 1** Timeline of modern radar altimetry missions (published with the permission of CNES)

The era of high-precision satellite altimetry started in the early 1990s with a minimum of 2 altimeter missions flying in different orbits (Fig. 1). Topex/Poseidon (NASA/CNES, 1992–2006) provided the first SSH observations with 2–3 cm accuracy on a 10-day repeat cycle, followed by Jason-1 (2001–2013), Jason-2 (2008–2019), Jason-3 (launched in 2016), and recently Sentinel-6 Michael Freilich (launched in 2020), all on the same long-term climate monitoring orbit. Complementary space–time coverage over all surfaces has been available from the 1990s onwards, on a 35-day repeat cycle from ESA’s ERS-1&2 (1991–2000; 1995–2011) and Envisat missions (2002–2012), and the Saral/AltiKA (joint mission from CNES and ISRO from 2013), from the 17-day Geosat-FO mission (US Navy/NOAA, 1998–2008), and the 14-day repeat cycle from the HY-2A/B/C missions (CNES and China’s NSOAS, from 2011 onwards). All of these nadir altimeter missions are in conventional “low-resolution” mode (LRM) and have provided the cornerstone of our ocean circulation observing system over the last 30 years.

The satellite radar altimetry measurement technique is based on an active radar emission at microwave frequencies from the satellite platform. The following description is mainly derived from Frappart et al. (2017). A more detailed description can be found in Chelton et al. (2001), Frappart et al. (2017), and on the AVISO+ website<sup>1</sup> and in the Radar Altimetry Tutorial<sup>2</sup> which is part of the Broadview Radar Altimetry Toolbox (BRAT).

Basically, the radar sensor emits an electromagnetic pulse in the nadir direction (vertically downwards) and precisely measures the two-way travel time of the signal ( $\Delta t$ ) between the satellite and the reflecting surface. Given the known speed of light in a

<sup>1</sup> <https://www.aviso.altimetry.fr/en/techniques/altimetry.html>.

<sup>2</sup> <http://www.altimetry.info>.



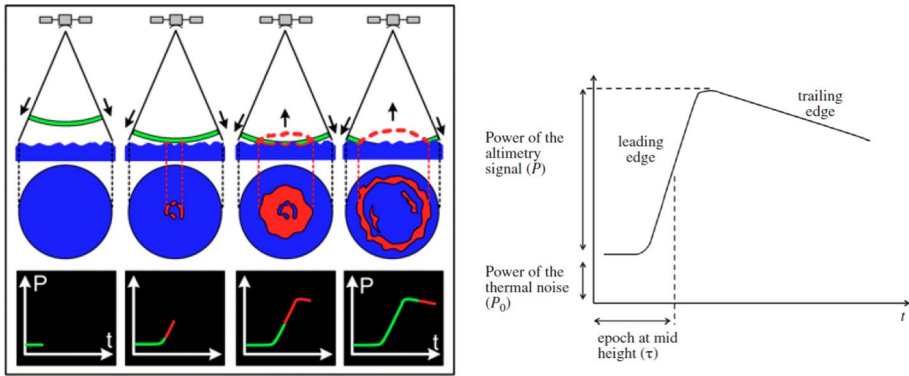


**Fig. 2** (left) Schematic of a time series of a radar pulse. In green, the outgoing radar pulse before it reaches the surface, in red, the pulse reflected from an ocean surface with waves received back at the sensor. The bottom panels show the radar power received at the sensor over time. (right) The main waveform parameters marked are derived from the Brown model used to determine the different altimetric geophysical parameters over the ocean. (Credits: CNES)

vacuum,  $c$ , the distance or range,  $R$ , between the sensor and the reflecting surface, such as the ocean, can be given by:

$$R = \frac{c\Delta t}{2} - \sum_i \Delta R_i \tag{5}$$

where  $\Delta R_i$  represents the sum of the corrections in the delay of the round-trip travel time, due to instrument, atmospheric or surface effects.

Although the emitted signal has a short duration, the return echo is longer since it is scattered back by many reflectors on the surface that are at slightly different distances from the radar. This return power that increases then decreases over time (Fig. 2) is called a “waveform” that has a characteristic shape that can be described analytically (for example, over the open ocean by the Brown (1977) model), or numerically. The waveform shape and amplitude provide information on the nature of the surface (ocean lakes or rivers, ice,...) and different geophysical parameters can be derived (sea surface height, significant wave height, wind speed, antenna mispointing; Fig. 2). For open ocean circulation studies based on the Brown model, the altimeter range ( $R$ ) corresponds to the time ( $\tau$  or epoch at mid-height) when the power received reaches the middle of the leading edge of the waveform. The power of the return signal gives information on the backscattering coefficient, from which the wind speed (amplitude, not direction) can be derived using empirical algorithms. Significant wave height is derived from the slope of the waveform’s leading edge, and the antenna mispointing from the trailing edge slope.

The Brown model is valid in spatially homogeneous conditions, such as the open ocean, where the characteristics of the water surface and the transmission through the atmosphere are uniform. Exceptions are in regions where the ocean backscatter or surface roughness varies rapidly (e.g., in low wind patches, under heavy rain cells, or near the coast when the ocean signal is polluted by the nearby land). Such events can be monitored and edited using the backscatter coefficient (e.g., Quartly et al. 2001; Dibarboure et al. 2014). Conventional radar altimeters provide measurements at a frequency around 10 Hz (T/P), 20 Hz (ERS, Jason, Envisat, CryoSat2) and 40 Hz (SaraI/AltiKa). Each of these measurements

is the (incoherent) sum of about 100 individual echos, and the summing helps reduce the measurement noise.

Figure 2 also shows a schematic of the pulses' "round" footprint on the ocean surface. For Jason-class altimeters, orbiting at 1336 km altitude, and for the pulses averaged over 1 s, this footprint is more oval in shape, being around 10 km alongtrack and 5 km cross-track (Chelton et al. 2001). The SSH signal and any noise effects contribute return power over the original footprint domain (50–70 km<sup>2</sup>), and then averaged over the 1-s time. The footprint size is determined by the pulse duration (3 ns  $\longleftrightarrow$  2 km for calm seas) but also depends on the sea state conditions, the altimeter frequency band, the antenna pattern and the satellite altitude. As an example, for a 3 m high significant wave height sea, the footprint crosstrack radius is around 3 km for Ka-band Saral/AltiKa at ~800 km altitude; 4.4 km for Ku-band Envisat at ~800 km altitude, and 5.5 km for Ku-band Jason at 1336 km altitude. The footprint size also increases in high seas as the sea state increases. For example, 10 m high SWH increases the footprint for Envisat to 7.7 km, and to 9.6 km for Jason (Chelton et al. 2001).

To obtain a precise estimate of the sea surface topography, the range has to be corrected for instrument corrections, atmospheric propagation delays (as the radar pulse passes through the wet and dry atmosphere, and due to interactions with the electron content in the ionosphere), and surface geophysical corrections. The details of this processing and an estimation of the errors can be found in (Chelton et al. 2001; Pujol et al. 2016 and Taburet et al. 2019). Before calculating geostrophic currents from the sea surface topography, surface geophysical corrections need to be applied to remove the effects of tides (ocean tides, solid earth tides, loading tides, and the pole tide), rapid atmospheric dynamical effects from wind and pressure forcing that are not resolved by the altimeter temporal sampling, and corrections for the geoid or mean sea surfaces.

### 3 Recent Extension to SAR Nadir Altimetry

A new generation of altimeters is starting to use nadir Synthetic Aperture Radar (SAR) and SAR-interferometry modes, including CryoSat-2 (ESA), where these different modes are acquired regionally. The first global nadir altimetry missions operating in SAR mode are the Sentinel-3A/-3B series of the Copernicus Programme of the European Union, built and launched by ESA and jointly operated by ESA and EUMETSAT since 2016. The global SAR altimetry coverage has been recently enhanced by the launch of the reference climate mission Sentinel 6A-Michael Freilich which operates in an interleaved LRM-SAR mode (ESA, EUMETSAT, NOAA, CNES, and NASA), also part of Copernicus. The first global coverage with a wide-swath SAR-interferometric altimetry mission will be SWOT—Surface Water Ocean Topography, launched in December 2022, aiming to study the 2D fine-scale ocean circulation and terrestrial surface waters, jointly developed by NASA and CNES, with contributions from the Canadian Space Agency (CSA) and United Kingdom Space Agency (UKSA).

The main interest of the SAR processing is to provide a greatly reduced footprint (less than 5 km<sup>2</sup>) compared to conventional LRM measurements having a footprint size of more than 100 km<sup>2</sup>. This gain in spatial resolution is in the direction of displacement of the satellite (alongtrack). Delayed Doppler/SAR altimetry exploits a coherent processing of groups of transmitted pulses in order to zoom in on a smaller alongtrack bin (Raney 1998; Boy

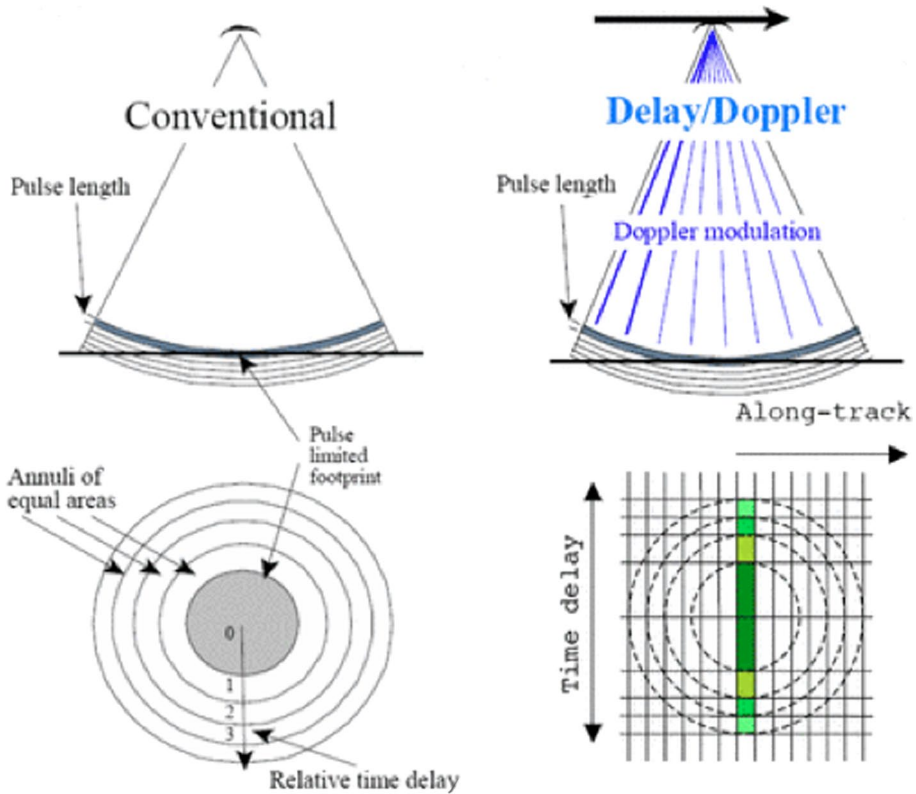


**Fig. 3** (left panels): Schematic of conventional LRM pulse-limited altimetry showing the concentric annuli of pulses being reflected back to the satellite, and contributing to the steady increase in power over the Brown waveform. (right panels): SAR uses a combination of the range information and the time delay. Here the circles represent the iso-range contours, and vertical lines the iso-doppler contours). The horizontal line is the trajectory of the satellite. (Courtesy of R.K. Raney, Johns Hopkins University Applied Physics Laboratory)

et al. 2017; Egado and Smith 2017; Frappart et al. 2017). Although the SAR processing is complex, the basic principle is based on the Doppler effect due to the moving satellite.

As the satellite travels horizontally, the Doppler shift is zero for the scattering point at nadir, but it increases almost linearly with the alongtrack distance between the scatterer and the nadir point. Figure 3 shows a schematic of this effect: the straight lines correspond to contours of equal linear Doppler shift. The circles are a selection of contours of equal range seen from the radar. The satellite is moving to the right along the track in this schematic. In essence, the SAR processing identifies the exact position of the return power and removes the power coming from all the vertical bands shown on Fig. 3 except from the central band (called the zero Doppler band) whose width is typically 340 m. This is then repeated for the adjacent Doppler bands to form a stack of waveforms.

As the satellite moves alongtrack, the same vertical band in Fig. 3(d) can be observed many times from the front of the round footprint, then the center, then the back. A multi-looking technique is used in the SAR processing, taking the sum of the contribution of many co-located vertical bands during a 2 s period, instead of just analyzing the millisecond

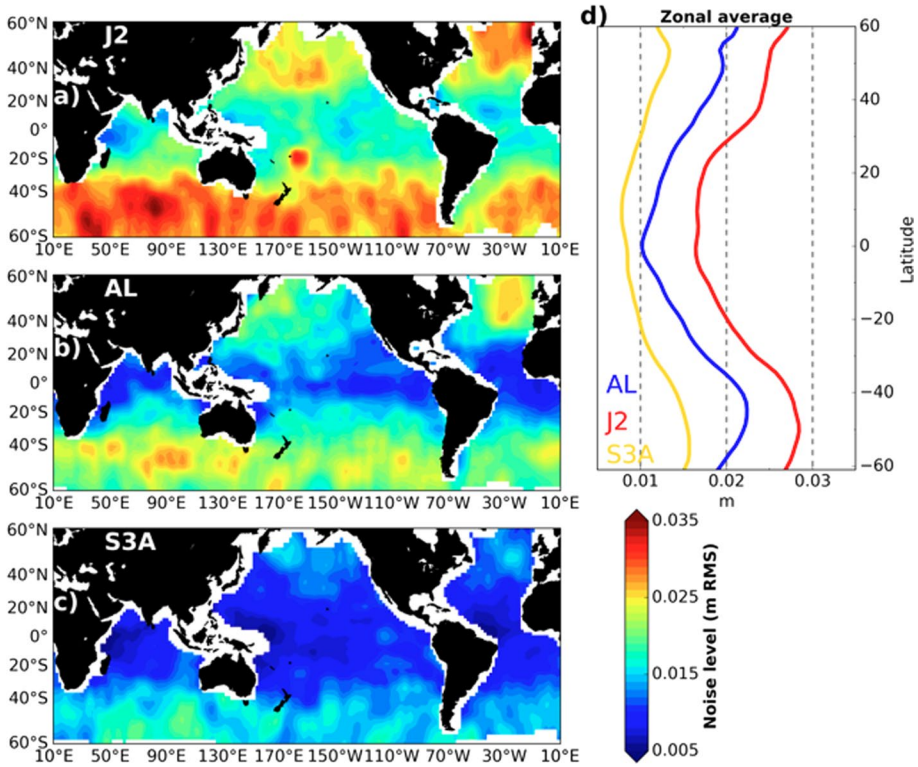


**Fig. 4** Global distribution of noise floors (in m RMS) computed inside the spectral wavelength range 15–30 km for **a** Jason-2, **b** AltiKa and **c** Sentinel-3A. (d) Zonal average of the error levels plotted in left hand panels (from Vergara et al. 2019)

observation from individual pulses. The advantage of this “stacking” within the SAR processing is that the averaged return signal (and integrated noise) is thus concentrated in the smaller central zero Doppler band, being 340 m alongtrack and ~5 km across track. In comparison, the convention LRM mode has the signal and noise integrated over the spherical diameter surface (Fig. 3c) whose footprint size varies depending on frequency, altitude, and surface roughness conditions. The SAR processing gives a more focused signal, and a much smaller noise level, since the noise is integrated over a smaller surface area, with less sensitivity to sea state (though impacted by swell). It can also approach closer to the coast or islands or sea ice, with fewer perturbations to the radar signal when the ground track is perpendicular to the coast/sea ice boundary.

We can estimate how the noise level varies between different altimeter missions and technologies based on global wavenumber spectral analysis of the alongtrack altimeter data (e.g., Xu and Fu 2012; Vergara et al. 2019). For each different altimeter mission, wavenumber spectral analysis of the 1 Hz alongtrack data shows a relatively flat noise floor below about 30 km in wavelength, due to this measurement noise returned over the footprint size. Figure 4 shows the global distribution of noise levels estimated from wavenumber spectra for three different altimeter technologies: Jason-2 in Ku band at 1336 km altitude, Saral/AltiKa in Ka-band at 800 km altitude, and Sentinel-3 in SAR mode at 814 km. As noted in Sect. 2, the Jason footprint size is largest, giving a wider

field of view of the noisy return signal, which is strongly impacted by the higher sea state at higher latitudes (Fig. 4a). Saral/AltiKa is also in conventional LRM mode but with a smaller altitude, more focused footprint and lower noise (Fig. 4b). The delayed-Doppler SAR processing on Sentinel-3 leads to the lowest noise on a global average (Fig. 4c), see Rieu et al. (2021). These noise patterns also vary seasonally, mainly related to sea state variations (Dufau et al. 2016; Vergara et al. 2019).

Over the last two decades, there have been important advances in the processing and reprocessing of the alongtrack altimeter data from all missions, and also in the quality of the multi-mission mapping by DUACS/AVISO, used in most oceanographic studies. Although the mesoscale band is the most energetic component of sea level, small-scale errors and noise are factors which limit our observation of the smaller mesoscales. The choice of editing, filtering or mapping can also impact on the ocean signals we can observe. There have been many improvements in the quality of these alongtrack data, including the editing and filtering steps and error estimation, as described in detail by Taburet et al. (2019) and aided by the ESA Climate Change Initiative Sea Level effort for open ocean studies (Ablain et al. 2015). Specific processing has also been developed in the coastal regions (see Laignel et al., 2023 for a review). Prior to mapping, the different altimeter missions are cross-calibrated against a reference mission (T/P-Jason series) to remove biases, and then a second time to reduce any residual long wavelength orbit errors (Pujol et al. 2016). Corrections are applied and sea level anomalies are calculated relative to a reference surface—either a precise time-mean alongtrack profile (for the missions on a long-term repeating track) or a gridded 2D mean sea surface product (for the new missions or non-repeating missions). All of these steps have a strong impact on the sea level anomalies and the derived geostrophic velocities.

Multi-mission merged sea level anomaly maps are then constructed for ocean studies, where the alongtrack data are suboptimally interpolated onto a fixed grid, using Gaussian spatial and temporal decorrelation functions (Ballarotta et al. 2019). The most recent DUACS maps based on delayed-time 2018 processing uses more than 25 years of multi-mission data (Taburet et al. 2019). New altimetry standards and geophysical corrections are regularly updated, the data selection has been refined, and optimal interpolation parameters have been tuned with 5–10% improvements in the coastal and regional seas, for both sea level and geostrophic currents.

The mean wavelength resolution of these gridded products varies from 100 km at high latitudes, to 200 km at mid latitudes, and reaches 800 km in the equatorial band (Ballarotta et al. 2019). A comparison with the alongtrack data shows that, in the 65–300 km mesoscale band, around 40% of the mesoscale variability is missing in these gridded products, mainly associated with the smaller mesoscale signals (this depends very much on latitude) (Pujol et al. 2016). There is reduced alongtrack filtering in the more recently reprocessed products, and in consequence, additional signals are now observed, associated with residual internal tide signals in both the alongtrack and mapped products (Ray and Zaron 2016; Dufau et al. 2016). As we reduce the altimetric noise, and resolve more small-scale structures, the separation and identification of internal tides and internal waves becomes more critical (see Sect. 9 on tides). Despite the progress in improving the alongtrack signal-to-noise, observations of the smaller mesoscale circulation in the open ocean, regional seas and at higher latitudes are limited today by the remaining alongtrack noise and the altimeter ground track sampling.

## 4 Future Observations with SWOT Wide-swath SAR-interferometry Altimetry

The SWOT SAR-interferometry wide-swath altimeter mission launched in December 2022 is designed to provide global 2D SSH data over two 50 km wide swaths with 2 km pixels, resolving spatial scales down to 15–20 km, for a 2 m high significant wave height (Fu et al. 2012; Fu and Ubelmann 2014); these values vary depending on the sea state (Wang et al. 2019a). These SSH observations will fill the gap in our knowledge of the 2D dynamic height variations in the 15–200 km wavelength band. These scales are not observed today with multi-mission altimeter maps in the open ocean, and these scales dominate in the coastal and regional seas and at high-latitudes. SWOT will also provide the fine-scale 2D horizontal gradients of SSH and their derived geostrophic currents, which are important for the ocean horizontal circulation and kinetic energy budget, but also for driving energetic vertical velocities and tracers transports (Levy et al. 2012; Balwada et al. 2021).

As the name suggests, the Surface Water and Ocean Topography (SWOT) mission brings together two scientific communities—oceanographers and hydrologists. For the hydrology community, SWOT SAR-interferometric data will enable the observation of the surface elevation of lakes, rivers and flood plains, and will provide a global estimate of discharge for rivers > 100 m wide, and water storage for lakes > 250 m<sup>2</sup>. SWOT will also provide unprecedented observations in the coastal and estuarine regions, forming a continuum of consistent ocean coastal hydrology observations. The science objectives covering all disciplines are outlined in the SWOT Mission Science Document (Fu et al. 2012), and an update on the ocean objectives and measurement system is given in Morrow et al. (2019).

### 4.1 SWOT Measurement Principle

Here we provide a brief overview of the SWOT Synthetic Aperture Radar Interferometric (SARIn) measurement system, based on the description in Frappart et al. (2017). A more complete description is given in Rodriguez et al. (2017). SARIn has been used extensively over the past three decades for fine resolution mapping and measuring changes of the surface of the Earth. The principle is to combine two SAR images of the same place on the ground taken from two distinct positions of the radar  $A_1$  and  $A_2$  separated by a distance  $B$  called the baseline (see Fig. 5). This figure is drawn in the plane orthogonal to the satellite speed vector, the line  $A_1, A_2$  is then in the across-track direction. This explains the name crosstrack interferometry.

In the past, the two images were standard SAR images taken at two different times for successive overflights of the same region by the same radar. The incidence angle (or look angle  $\theta$  shown on Fig. 5) was typically between 20 and 40 degrees. In the case of SWOT, the satellite carries two antennas separated by a baseline  $B$  of length 10 m, and the two SAR images can be obtained simultaneously. The look angle  $\theta$  is much lower for SWOT (between  $0.6^\circ$  and  $4^\circ$ ) so these measurements are near-nadir SAR-interferometry.

A radar pulse is directed to one swath, and the scattered return is received at both antennas. This is then repeated on the other swath. The two return radar measurements can be used to determine the range  $r_1$  and  $r_2$  with a range resolution of 0.75 m for SWOT. The instruments also measure the phase of the signal and the interferometric phase  $\Phi$  can be computed with great accuracy. However, the phase difference between the two return signals has an ambiguity of  $2\pi$  that is removed by a processing called phase unwrapping

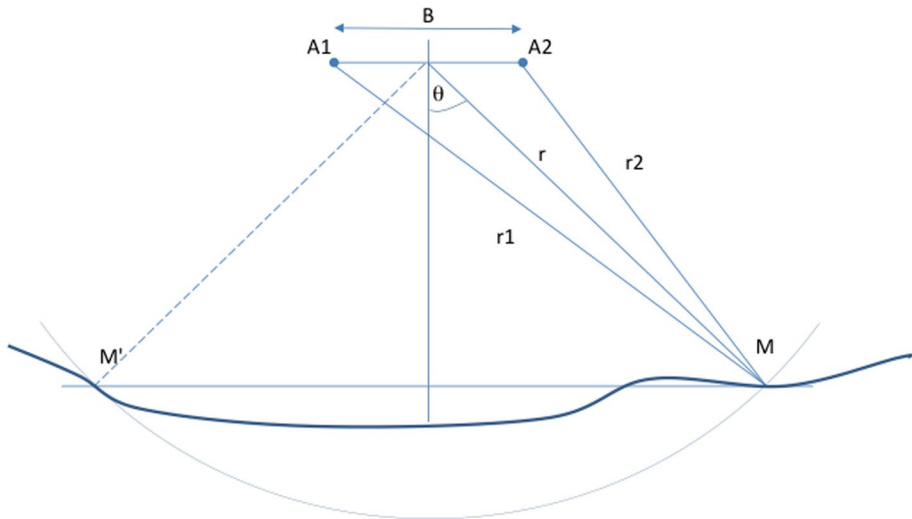


**Fig. 5** Principle of crosstrack interferometry (after Frappart et al. 2017)

(Rodriguez et al. 2017). After phase unwrapping the absolute phase  $\Phi_a$  is known and the differential range  $r_1 - r_2$  and the incidence angle,  $\theta$ , can be deduced. Once the range  $r$  and the angle  $\theta$  are known, the position in 3D space of the point  $M$  can be obtained. This process is called geolocation and height retrieval. This is a very simplified description; further details are given in Rodriguez et al. (2017).

The processing of the image formation is done independently for the left and the right swaths of SWOT. Note that the signal coming from the point  $M'$  is symmetrical with  $M$  and is thus measured at the same range as the signal coming from  $M$  (Fig. 5). This leads to an ambiguity in the detection of signals coming from the left and right swath that needs to be removed at the instrument level. For SWOT, this is done using the right and left antenna patterns and using different polarization of the signals (One pulse is emitted in H-polarization, the next in V-polarization, etc.). For the SARIn mode on CryoSat-2 used over the steep polar ice-caps and ice-shelves, the goal was to provide measurements at nadir and there is no device to remove the left–right ambiguity. So CryoSat-2 SARIn observations are not well adapted for flat ocean observations, but capture well the steep terrain slopes in the crosstrack direction on a polar ice-cap.

SWOT uses SAR processing to refine the alongtrack resolution of the return signal, and the interferometric processing refines the crosstrack resolution. The SWOT SAR-KaRIn instrument (see Fig. 6) provides a basic measurement resolution of 2.5 m alongtrack, and ranging from 70 m in the near-nadir swath to 10 m in the far swath. Over the terrestrial surface waters, an onboard pre-summing is performed, and data are downloaded at 5.5 m resolution alongtrack, with the maximum crosstrack resolution. Full interferometric processing is then performed on the ground. Over the 70% of the Earth's surface covered by the oceans, the huge amount of data produced cannot be downloaded from the satellite at its maximum resolution. Instead, so-called “low-resolution” data are pre-processed onboard, and building blocks of 9 interferograms at 250 m posting (and 500 m resolution) are downloaded from each antenna. Other parameters that are useful for the surface waves and front detection, such as the 250 m resolution SAR backscatter images, are also

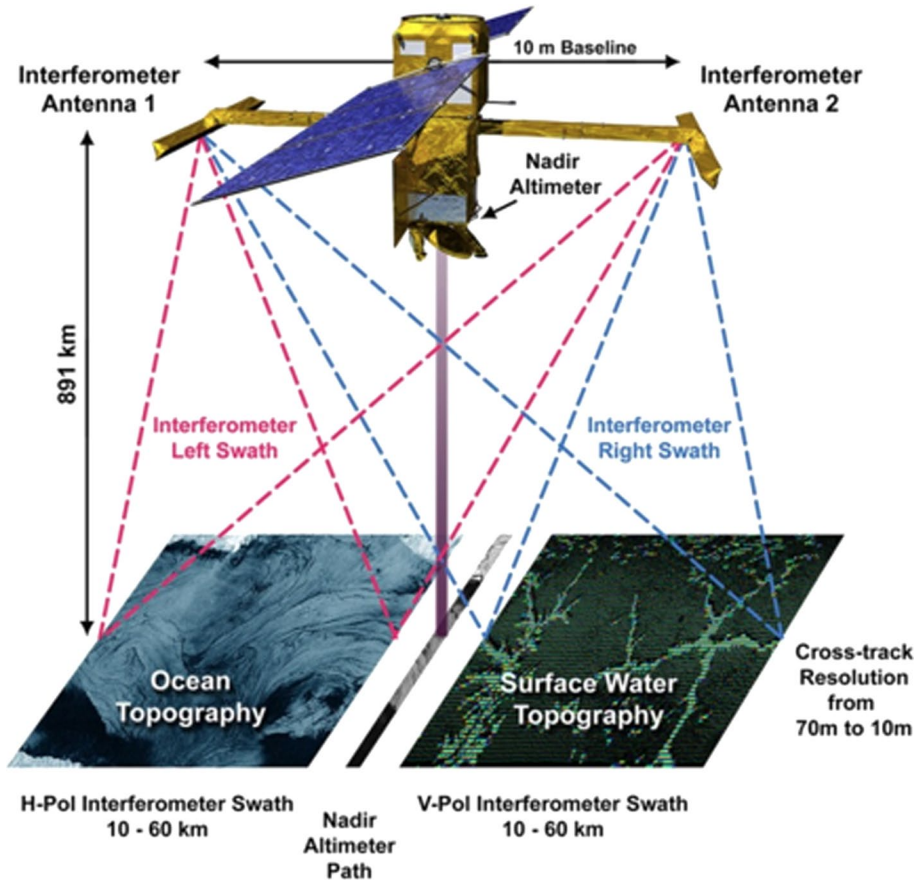


**Fig. 6** Schematic of the SWOT measurement technique using the KaRIn instrument for SAR-interferometry over the two swaths, and a Jason-class nadir altimeter in the gap. (Courtesy of K. Wiedman for NASA-JPL)

downloaded. These data are combined through the geolocation and height calculation into a  $250 \text{ m} \times 250 \text{ m}$  expert SSH product with higher errors in swath coordinates, and a standard  $2 \text{ km} \times 2 \text{ km}$  product in geographically fixed coordinates. The error estimate of these  $2 \text{ km}$  averaged data is  $2.5 \text{ cm}/\text{km}^2$  (Chelton et al. 2019), more than an order of magnitude smaller than conventional Jason-class measurements.

## 5 Mean Ocean Circulation from Space

Ocean currents arise when water parcels are moved by atmospheric forcing (winds, solar heating, precipitation), freshwater input from rivers or ice melt, and tidal-gravitational effects from the Moon and the Sun around an equilibrium state where the only acting force is the Earth's gravity. Due to the inhomogeneous distribution of mass in the Earth interior, this equilibrium state, called the geoid, is a surface topography with hollows and bumps of an amplitude of  $\pm 100 \text{ m}$ , as measured relative to a reference ellipsoid, i.e., a theoretical, mathematically defined topographic surface that approximates the geoid. The sea level



departure from the geoid caused by the above-mentioned external forcing is called the Absolute Dynamic Topography (ADT). Under the geostrophic approximation, when a difference in Absolute Dynamic Topography occurs between two locations in the ocean, the resulting geostrophic current flows perpendicular to the sea slope, to the right in the northern hemisphere and to the left in the southern hemisphere.

Mean ocean circulation is in geostrophic balance to the first order. It can be readily obtained from the combined knowledge of the mean sea level above the reference ellipsoid, and the geoid height relative to the same reference ellipsoid, both quantities being measurable to a certain extent from space.

Satellite altimeter sensors provide alongtrack measurements of the sea level above the reference ellipsoid. Some altimeter missions have an exactly repeating cycle (i.e., the altimeter passes above the same point at regular intervals: around 10 days for the TOPEX–Jason–Sentinel-6 satellite series, 27 days for the Sentinel-3 series), and the Mean Sea Surface (MSS) above the reference ellipsoid can be obtained by averaging altimeter measurements over a long period. Today, state of the art altimetric Mean Sea Surfaces have a centimetric accuracy at spatial scales of a few tens of kilometers (Pujol et al. 2018), based on a combination of longtime series of repeat-track data plus a large amount of data in new geographical regions from recent geodetic orbit altimeter missions. These geodetic mission data have smaller inter-track distances, but fewer or no repeats leading to some ocean variability contamination in the mean.

From 2000 onwards, important technological and conceptual steps have been made to compute the Earth's gravity field from space, leading to the launch of dedicated space gravity missions such as CHAMP (2000), GRACE (2002), and GOCE (2009). Today, the geoid is measured from space with centimetric accuracy at scales greater than 100 km. At first order, the geoid can be considered stationary (it does not change with time), so by subtracting the geoid from the altimeter MSS, we can retrieve an accurate estimate of the Mean Dynamic Topography, and hence, by geostrophy, of the mean ocean currents. Using this approach, the mean ocean circulation can be retrieved for spatial scales larger than 100 km.

However, geostrophic currents in the ocean occur at shorter spatial scales than this, in particular at high latitudes and in coastal areas, where the first Baroclinic Rossby Radius of Deformation, a commonly used proxy for the validity of the geostrophic approximation, decreases down to a few kilometers (Chelton et al. 1998). Various methods have therefore been developed in order to increase the resolution of the ocean Mean Dynamic Topography (MDT), and the corresponding mean geostrophic circulation. These methods can be divided into two main categories. In the first method, the geoid resolution is improved, and then a higher resolution MDT is computed by direct combination. In the second method, a large-scale “geodetic” MDT (i.e., computed from differencing an altimetric MSS and a geoid model) is first computed and further improved using external oceanographic data to resolve the shorter scales.

In the first case, the quantity to improve is the geoid. This can be done using in situ gravimetric data. Since these data are often limited in spatial extension, this approach results in local to regional improvement of the geoid. Global improvement can be achieved by exploiting the fact that the shortest spatial scales of the altimetric Mean Sea Surface are mainly due to the shortest spatial scales of the geoid, and can therefore be used to enhance this latter. For instance, both in situ gravimetric data and altimetry-derived gravity anomalies have been used to compute the EGM08 geoid model (Pavlis et al. 2012) at a spatial resolution of around 8 km.

In the second case, to improve the geodetic MDT resolution, estimates of the mean heights and mean geostrophic velocities are built from available in situ measurements of

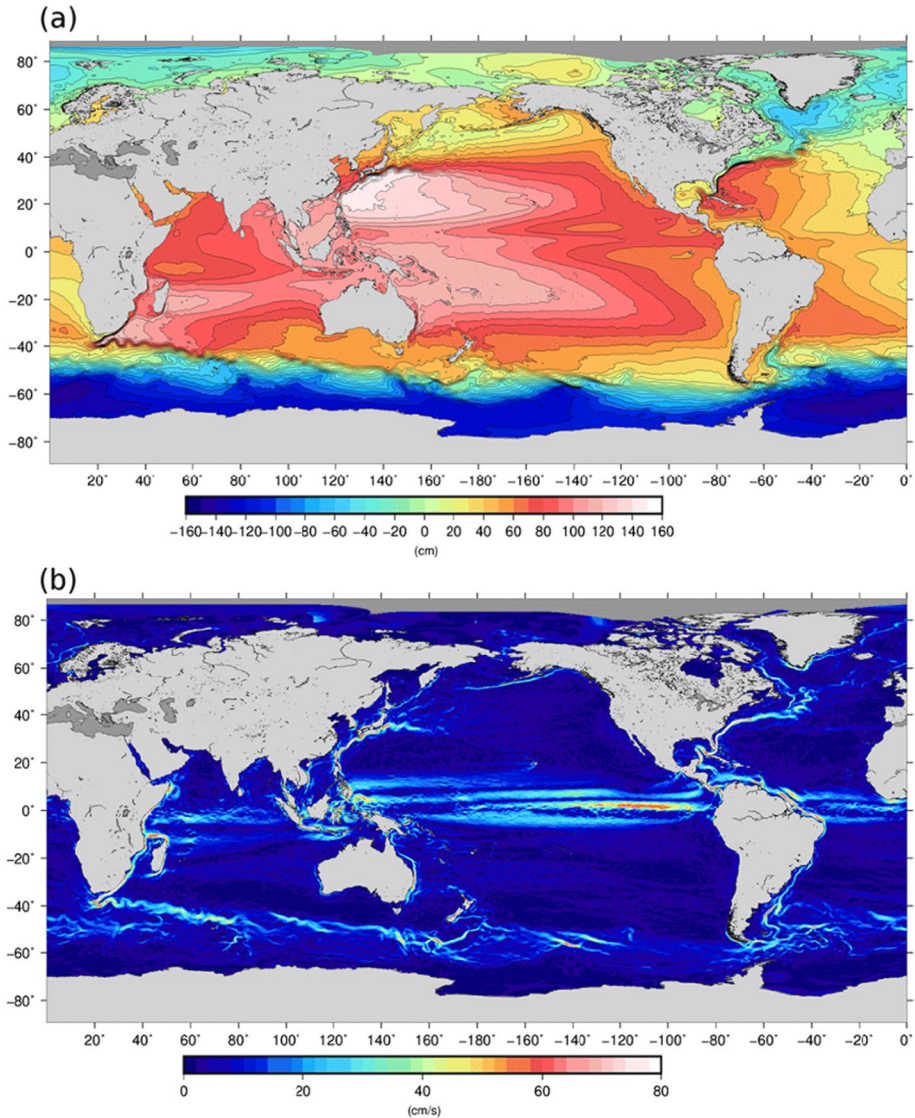


**Fig. 7** The CNES-CLS18 **a** Mean Dynamic Topography and **b** corresponding mean geostrophic currents as calculated by Mulet et al. (2021)

ocean dynamic height and current velocities, from which the temporal variability measured by altimetry has been removed (Rio and Hernandez 2004, Maximenko et al. 2005). In situ data are processed to make them consistent with the physical signal measured by altimetry: Absolute dynamic heights are reconstructed from the in situ steric dynamic heights, and the geostrophic component of the ocean currents is extracted from the drifter velocities. The resulting mean velocities and heights are then used to improve the large-scale geostrophic MDT. Recent global combined MDTs resolve spatial scales down to 25–50 km with 5–10 cm accuracy. Figure 7 shows the CNES-CLS18 MDT and corresponding geostrophic

mean circulation calculated by Mulet et al. (2021) on a 1/8 grid. All major ocean currents are clearly resolved (Gulf Stream, Agulhas, Kuroshio, Antarctic Circumpolar current) with maximum intensities greater than 1.5 m/s. Using a similar approach, mean currents can be estimated at even higher spatial resolution at local/regional scales where sufficient spatial density of in situ measurements is available, such as High-Frequency Radar (Caballero et al. 2020).

## 6 Large-scale Ocean Variability from Space

Our knowledge of the basin-scale ocean circulation has advanced greatly over the last 30 years due to the combination of satellite altimetry products and major in situ programs designed to better quantify the ocean's vertical structure with dedicated hydrographic data. The strength of satellite altimetry is its global coverage with continuous and consistent sampling, enabling the synthesis of in situ observations into a basin-wide global estimate of the state of ocean circulation over decadal scales.

In the 1990s, the World Ocean Circulation Experiment (WOCE; <https://www.ncei.noaa.gov/archive/accession/NCEI-WOA18>) started a decade-long survey of top to bottom hydrographic sections across the world oceans, completed by more regular upper ocean in situ sampling. This quantified the global mean ocean state and its slow variations. This first major survey continued over the next decades with full-depth in situ repeat sections and upper ocean sampling within the WRCP CLIVAR program ([www.clivar.org](http://www.clivar.org)). A major breakthrough in the ocean in situ spatial–temporal sampling came with the Argo program (<https://argo.ucsd.edu/>), providing 0–2000 m profiles every 10 days and at roughly 3° (300 km) spacing, with full global coverage achieved from 2005 onwards. Throughout these 3 decades, satellite altimetry and other surface data sets (e.g., SST, surface drifters) completed this large-scale monitoring of the ocean circulation by providing full geographical coverage and the temporal evolution between these in situ data points.

Monitoring the ocean transport of mass, heat, salt, freshwater, and other tracers has always been a crucial part of understanding the basin-scale ocean circulation and its variations, with impacts for the global thermohaline circulation and climate. Dynamic height from satellite altimetry can be analyzed against in situ dynamic height and then related to transport variability across the basin, as described in the Atlantic Ocean review paper by McCarthy et al. (2020). The Atlantic Meridional Overturning Circulation has been observed with moorings and ship in situ data at a number of basin-wide sections. Regular altimetric sampling can be combined with ship-based hydrographic profiles or with mooring measurements to produce a continuous transport time series (see Fig. 8), and to evaluate the ability of ship-based techniques to capture the synoptic and interannual variability (Gourcuff et al. 2011; Mercier et al. 2015; Frajka-Williams et al. 2019). The North Atlantic has been in a cooling period since the mid-2000s, and during this time altimetry has shown that the subpolar gyre has been cooling, strengthening and widening resulting in negative sea level trends there, and winds along the eastern boundary have become predominantly from the north, which drives a slow-down in the shelf and coastal sea level rise (Chatif et al. 2019). During an earlier warming period from the early 1990s to the mid-2000s, the reverse occurred.

Basin-scale overturning circulation studies are also undertaken using a combination of density anomalies derived from Argo floats, regressed against satellite altimetry sea surface height anomalies (e.g., Willis 2010). Although Argo data are only available from 2000

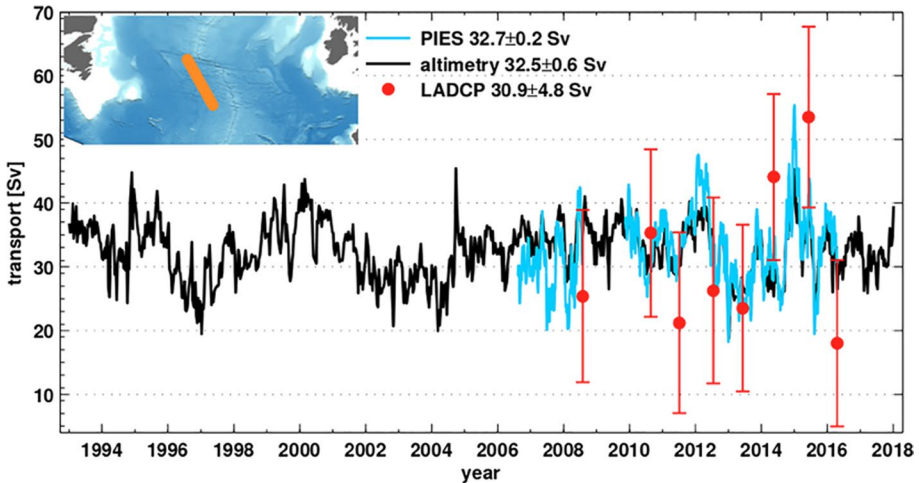


**Fig. 8** Bimonthly volume transport time series of the North Atlantic Current (from  $47^{\circ}40'N$  to  $53^{\circ}N$ ) from the western into the eastern Atlantic relative to 3,400-m depth (updated from Roessler et al. 2015). Blue: estimates based on the moored PIES. Black: based on the correlation between the altimeter surface velocity and the PIES transports. Red dots: transport estimates calculated from LADCP profiles taken along the PIES array. The vertical red lines denote the uncertainties. The mean of all three methods agree within their uncertainties (after McCarthy et al. 2020)

onwards, once a stable regression has been established, a time series can be reconstructed over the entire altimetric 3-decade period. A key point is to set the reference velocity for the dynamic height equation; one solution is to derive a barotropic adjustment at 1,000 m based on the subsurface drift of the Argo floats (Willis and Fu 2008). Three-dimensional geostrophic velocity fields have also been calculated from the gridded satellite altimetry surface heights and a vertical relation derived from Argo float data by Schmid (2014), again the reference velocity is derived from the deep float trajectories. An alternative is to set the reference velocity from the surface absolute geostrophic currents from altimetry, and project the currents vertically using the thermal wind equation (Eq. 4) using the time-varying density field at depth from Argo (Mulet et al. 2012). These examples are from the Atlantic Ocean but transport studies derived from satellite altimetry and in situ data have been performed in many different ocean basins. The joint use of long-term basin-wide altimetry data, surface forcing fields, and in situ data are critical for understanding the mechanisms that produce these transport variations, and helping us understand the ocean circulation's role in climate.

A major contributor to basin-scale ocean adjustment is from planetary waves, influenced by the Earth's rotation, such as Rossby and Kelvin waves. Limited observations of these waves had been revealed from shipboard, mooring and island measurements (e.g., Wunsch and Gill 1976). Over the past decades, satellite SSH observations have provided the necessary spatial and temporal sampling to allow significant advances in our knowledge of these basin-scale waves.

Weekly or daily maps of satellite altimetry data have allowed us to track the (mainly) westward propagation of Rossby waves across ocean basins, and the eastern propagation of equatorial Kelvin waves, clearly shown through Hovmöller diagrams. Frequency–wave-number spectra of altimetric SSH also show that variability is concentrated over a band of negative wavenumbers, indicating westward propagation (Fu and Chelton 2001). In the

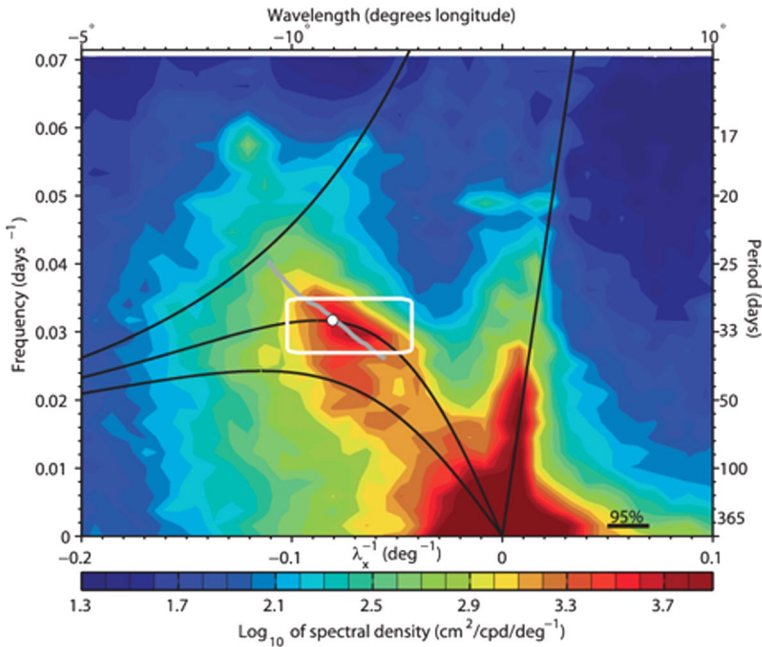


**Fig. 9** Zonal wavenumber–frequency spectrum of SSH, averaged over 7°S–7°N. The white box indicates TIW spectral peak near periods of 33 days and zonal wavelengths of 12°–17° of longitude. The four black curves are the dispersion curves of linear equatorial wave theory for the first baroclinic mode Kelvin, mixed Rossby–gravity, and Rossby waves. A more realistic theoretical dispersion curve for the TIWs, derived by Lyman et al. (2005) from a linear stability analysis, is indicated by a thick gray curve. The white circle indicates the wavenumber and frequency of the most unstable mode of the Lyman et al. (2005) analysis. The 95% confidence interval should be measured against the color scale (after Farrar 2011)

late 1990s, the mid-latitude westward propagating signals were interpreted against linear Rossby wave theories (Chelton et al. 2011). However, there were discrepancies. The observed phase speed was faster than that predicted from conventional linear theory. Theoretical developments followed to try and explain the observations, including the effects of the background stratification introducing vertical shear of a mean current and bathymetric steering effects. More recent interpretations highlight the “non-dispersive” nature of the propagation, more likely due to nonlinear eddy effects (see Wunsch 2010; Chelton et al. 2011). This will be discussed more in the following section on mesoscale processes.

Tropical dynamics are complicated by the rapidly diminishing Coriolis force toward the equator, leading to the rich structure in the frequency-wavenumber spectrum of SSH shown in Fig. 9, computed from altimetry data in a latitude band of 7°S–7°N across the tropical Pacific (Farrar 2011). The dominant SSH spectral power is well aligned with the theoretical dispersion relation for eastward propagating Kelvin waves (the black straight line in the side of positive wavenumbers), the mixed Rossby-gravity waves, and the first and second modes of the westward propagating baroclinic Rossby waves (the black curves from the top to the bottom with negative wavenumbers). In addition to the strong variance of the Kelvin waves and the baroclinic Rossby waves at large wavelengths and low frequencies, a prominent band enclosed by the white rectangle covering periods of ~33 days and wavelengths of 12°–17°, represents the tropical instability

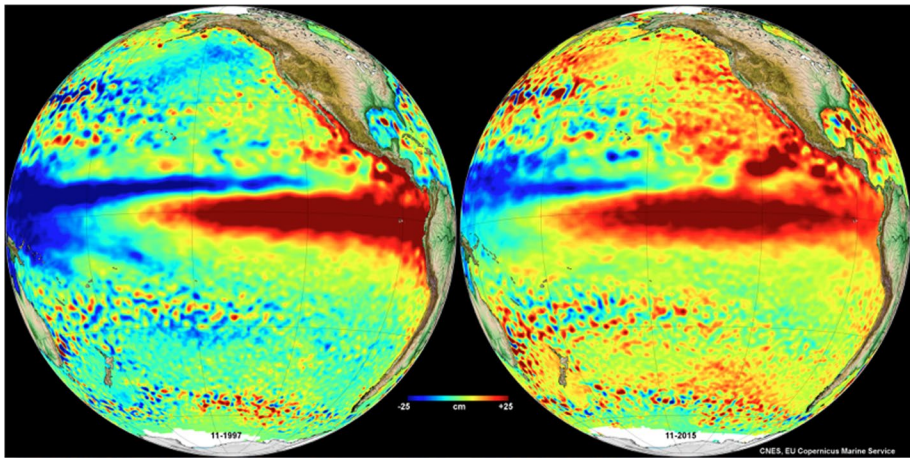


**Fig. 10** Altimetric sea level anomalies during the 1997 (left) and 2015 (right) eastern Pacific El Niño events. (CNES / EU Copernicus Marine Service)

waves (TIW). These waves were first detected from satellite observations of sea surface temperature (Legeckis 1977). Satellite altimetry observations have provided an unprecedented database for advancing the understanding of these waves (e.g., Lyman et al. 2005). The dispersion relation derived for the TIW by Lyman et al. (2005) from a stability analysis is shown by the gray line in the rectangle, with the white circle denoting the most unstable mode. Farrar (2011) demonstrated from SSH observations that the energy of these TIW radiates to the mid-latitudes in the form of barotropic Rossby waves, and Farrar et al. (2021) show that they reflect and refract off the complicated bathymetry in the North Pacific, leading to a complex pattern in SSH. This rapid barotropic Rossby wave variability is only revealed with specific mapping techniques, and is not well represented in the widely used AVISO gridded SSH data product due to the larger temporal decorrelation used in the standard objective mapping scheme. This should be modified in future versions. These planetary wave examples in the Pacific Ocean demonstrate how the basin-scale, regularly sampled SSH observations allow us to study the influence of the tropical perturbations on the mid-latitude ocean circulation; many other studies have addressed these waves in the Indian and Atlantic oceans.

The decadal global observations from space have revealed interannual and long-term changes in the ocean circulation. Satellite altimetry has captured the different flavors of the interannual ENSO events, from the strong perturbations in the Eastern Pacific caused by the 1997/98 and 2009 El Niños, to the central Pacific events, the so-called “Modoki” El Niño, which are more prevalent over the last 2 decades (see Capotondi et al. 2015; for a review). Although the ENSO variability is largest at the equator, there are strong atmospheric and oceanic connections to higher latitudes, and satellite altimetry allows us to monitor and interpret these extra-tropical variations. These ENSO events have a strong impact on global climate, but are themselves modified by long-term climate variations and climate change (e.g., Cai et al. 2014). Figure 10 shows the altimetric observation of the tropical and extra-tropical impact of the 1997 and 2015 eastern Pacific El Niños, occurring during different phases of the basin-wide Pacific Decadal Oscillation (PDO) with a strong signature in the ocean and atmospheric circulation.

The basin-wide PDO also impacts on the Kuroshio Current System, a major western boundary current at mid-latitude in the North Pacific. Qiu and Chen (2011) discovered a relationship between the PDO index and the characteristics of the Kuroshio Extension Jet east of Japan. During the positive phase of the PDO when the sea surface of the tropical Pacific is warm and that of the Northwest Pacific is cool, the Kuroshio extension jet becomes stronger. During the negative phase of the PDO, the jet becomes weaker. Qiu and Chen (2011) also found that the position of the jet moved northward during the positive phase of the PDO and southward during the negative phase. Thus, the Kuroshio Current System is part of a basin-wide ocean–atmosphere coupled system of decadal variability of the Pacific Ocean. The PDO-related SSH variations dominated the overall basin-wide SSH trends during the altimeter period (Hamlington et al. 2014). By removing the PDO patterns from SSH variations one can assess the decadal variation of SSH caused by global warming.

One of the big questions being addressed with the 30 years of satellite altimetry SSH observations is how the basin-scale variability we observe responds to atmospheric forcing, and which part of the variability is due to intrinsic internal ocean changes. For these studies, altimetric SSH data are carefully analyzed against different atmospheric forcing (wind, air-sea heat and freshwater fluxes), and the dynamics are also compared with realistic ocean circulation models (e.g., Vivier et al. 1999; Kelly et al. 2017; Frajka-Williams 2019). To determine the role of intrinsic or chaotic ocean variability, altimetric SSH is generally compared with a realistic model that is forced in two ways: by realistic interannual atmospheric changes or a climatological annual cycle. Penduff et al. (2011) compared altimetry with a  $\frac{1}{4}^\circ$  model and showed that the intrinsic contribution is particularly strong in eddy-active regions and within the  $20^\circ$ – $35^\circ$  latitude bands, whereas the atmosphere directly forces the interannual variability at low latitudes and in the eastern basins. This intrinsic ocean variability also impacts on regional sea level trends, with 40–45% of the global ocean areas dominated by chaotic variability (Llovel et al. 2018). Continued space monitoring of the global oceans and regional seas over decades can help us provide the precious observations of these complex interactions.

## 7 Mesoscale Ocean Variability from Space

The ocean circulation's most energetic component is at mesoscales, due to ocean eddies or isolated vortices, meandering currents or fronts, squirts, and filaments. Mesoscale processes are generally in quasi-geostrophic balance, the so-called “balanced motions” and can have spatial scales of 10–500 km in wavelength, and time scales of days to months. A number of review papers cover the early mesoscale studies with satellite altimetry by Le Traon and Morrow (2001), Fu et al. (2010), Morrow and Le Traon (2012), and Morrow et al. (2018).

Over the last three decades, satellite altimetry has provided global, high-resolution, regular monitoring of this energetic mesoscale variability. Since the early 1990s, the combination of two to up to six altimeter missions produced an accurate and detailed monitoring of the mesoscale variability, mainly via the AVISO/CMEMS gridded maps that resolve mesoscales varying from 100 km in wavelength at high latitudes, to 800 km in the tropics (Ballarotta et al. 2019), and with time scales exceeding 10–15 days. Three decades of daily altimetric gridded maps have provided the backbone of our analyses of ocean mesoscale processes, their role in regional and basin-wide ocean adjustment, in the ocean's

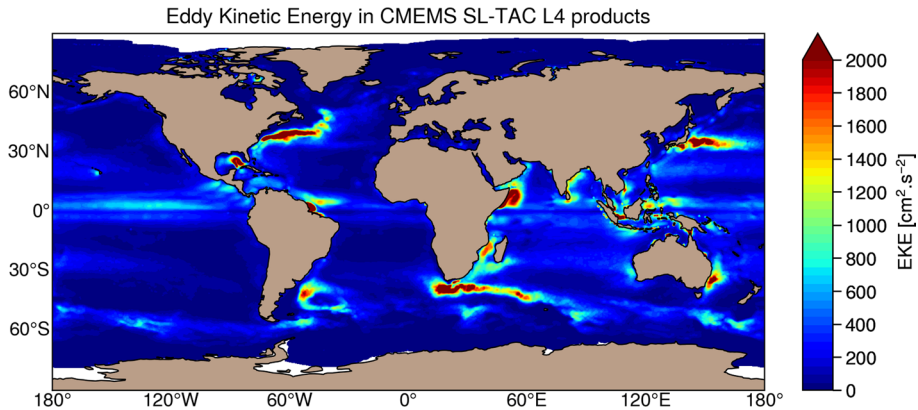


**Fig. 11 a** Mean ocean geostrophic eddy kinetic energy computed from delayed-time CMEMS SL-TAC Level-4 multi-satellite gridded altimetry products, for the period 1 January 1993 to 3 June 2020

energy cascade, and how they vary regionally and in interaction with larger-scale climate variations.

## 7.1 Eddy Kinetic Energy

Oceanic eddy kinetic energy (EKE) calculated from gridded satellite altimetry maps provides a powerful observational diagnostic to understand ocean circulation variability and to validate numerical models. EKE is larger in the energetic western boundary currents and along the Antarctic Circumpolar Current (See Fig. 11).

The long, multi-decadal time series of satellite data allows us to better understand the seasonal and interannual variations in EKE, the latter often linked to varying climate modes. Surface EKE is found to be maximum in summer over most of the subtropical gyres and Western Boundary Current regions in both hemispheres (Scharffenberg and Stammer 2010). This increase in the EKE may be due to seasonal changes in the horizontal gradients in the thermocline due to atmospheric forcing (Rieck et al. 2015), or to the inverse cascade of energy from the energetic winter mixed layer instabilities that develop at smaller scales in the mid-latitudes (Sasaki et al. 2014). Regional studies have highlighted the causes of the increased eddy variability along the Kuroshio Current's extension and mid-ocean subtropical Pacific and Indian jets due to seasonally and interannually varying instability processes (Qui and Chen 2005; Qui et al. 2014) and in the tropical regions impacted by the Indian and Asian monsoons, and by tropical instability waves (Farrar and Durland 2012). A near 30 year time series of altimetric EKE and satellite sea surface temperature gradients also show that the eddy field has strengthened at rates of 1.2–1.8% per decade globally, reaching rates of 5% per decade in the Antarctic Circumpolar Current (ACC) and 2.5% per decade in ocean boundary currents (Martínez-Moreno et al. 2021). Thus regions with energetic eddies are becoming more energetic.

One consideration for any long-term studies calculating interannual variations from altimetric maps is that the data processing changes and the number of missions included in the gridded data sets can vary, potentially modifying the gridded energy levels. Two products are available on AVISO: the two-satellite or C3S product that maintains consistent sampling over the 30 year period, mainly based on the long-term Jason orbit and completed



by a second mission on the ERS/Envisat/AltiKa or more recent Sentinel-3 orbit. A second multi-mission gridded product includes the maximum number of available missions but the quantity of data varies over time, from two missions in the 1990s, 3–4 missions in the 2000s and with more than 6 missions since 2016. The variations in EKE between these two products can reach 5–10 cm<sup>2</sup>/s<sup>2</sup> over the 30 year period, with stronger variations at mid to high latitude. In general, for long-term EKE or eddy tracking studies, it is recommended to use the consistent sampling over time from the 2-satellite configuration.

## 7.2 Tracking Ocean Eddies

Since altimetric SSH represents the depth-integrated density perturbations and barotropic movements, altimetry can track deep-reaching ocean eddies over months or years, even as their surface mixed layer is modified by air-sea interactions, and their signature in surface tracers fields is lost (e.g., SST, SSS, or ocean color). Nonlinear vortices can transport heat, salt, carbon, and other tracers in their core waters, with consequences for the mid-latitude transport of tracers (e.g., Dong et al. 2014; Zhang et al. 2014).

Different automatic eddy tracking techniques have been developed to study the propagation pathways of eddies at mid to high latitudes using mapped altimetric data. These can be based on the Okubu–Weiss parameter, the skewness of the relative vorticity; criteria based on sea level or velocity, wavelet decomposition of the sea level anomalies, or a geometric criteria using the winding angle approach (for a review of these techniques, see Souza et al. 2011). Depending on the technique used, there can be differences in the number of eddies detected, their duration and their propagation velocities (Souza et al. 2011). In the open ocean, sea level or velocity anomaly maps are often used, but in regions close to coasts, bathymetry or orographic effects, semi-permanent eddies can be generated that have a signature in the mean field. In this case, it is more robust to use the Absolute dynamic topography or velocity maps to track eddies (e.g., Pegliasco et al. 2021).

Altimetric eddy tracking has many regional applications but global analyses are also available (e.g., Chelton et al. 2007, 2011; Faghmous et al. 2015). The seminal work by Chelton et al. (2007; 2011) highlighted that sea level anomalies in the extra-tropics are largely non-dispersive, with characteristics closer to nonlinear vortices than Rossby waves. Yet approximately 75% of these vortices propagate westward at the speed of non-dispersive long Rossby waves. The remaining 25% are found in the strong eastward currents in the western boundary of the mid-latitude gyres and the Antarctic Circumpolar Current (see also Frenger et al. 2015), and drift eastward with the currents. A significant fraction (~20%) of eddies has lifetimes longer than 16 weeks traveling over an average distance ~550 km. Figure 12 depicts the trajectories of the long-lived eddies. There are roughly equal numbers of cyclonic and anti-cyclonic eddies. The lack of eddies in the tropical region is primarily due to their large and complicated size, fast speed, and the dominance of planetary waves, making the tracking technique ineffective. Outside the tropics, strong eddies, with amplitudes larger than 20 cm, are concentrated in the region of strong currents, and the eddy radius decreases with latitude as the Rossby radius of deformation decreases.

Tracking these larger mesoscale eddies in the altimetry data record allows the collocation of similar eddy features in other ocean parameters observed from space. For example, Gaube et al. (2015) analyzed sea surface wind vectors (from satellite scatterometer) and temperature (from satellite infrared and microwave radiometers) collocated over eddies detected with satellite altimetry. Their composites demonstrated eddy-like patterns of wind and temperature linked to ocean–atmosphere interaction at the eddy scales. Eddy currents

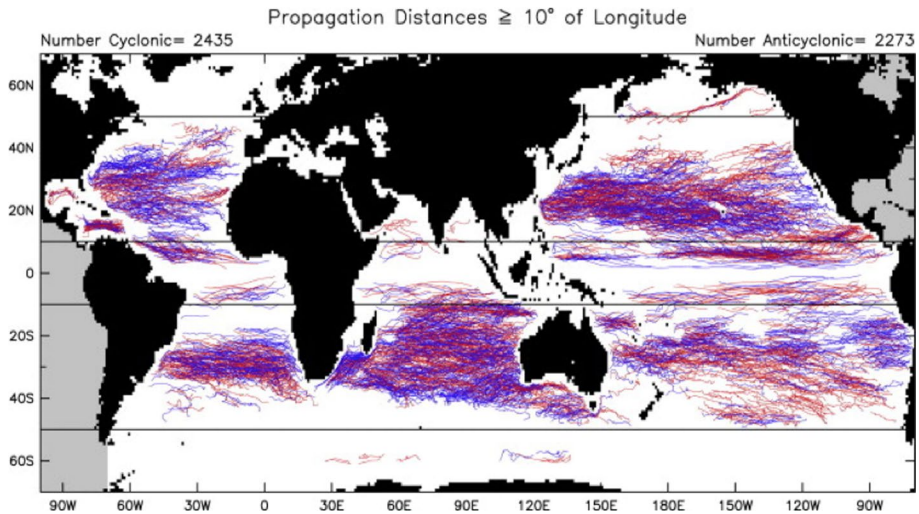


**Fig. 12** Global maps of the characteristics of eddies that were tracked for 16 weeks or longer in the first 16 years of the merged altimeter dataset (October 1992–December 2008) showing the trajectories of cyclonic and anti-cyclonic eddies (blue and red lines, respectively) (after Chelton et al. 2011)

create distinct structures of sea surface temperature and roughness, which in turn affects the wind patterns that feed back onto ocean currents via Ekman pumping (see Chelton and Xie 2010 for a review). Such self-sustained processes play a significant role in the dynamics of ocean circulation.

### 7.3 Ocean Mesoscale Fronts, Filaments and Strain

The ocean eddy field is highly turbulent and its evolving structure generates smaller eddies from barotropic, baroclinic and other instability processes. The fluid around these eddies is stretched and strained into fronts and filaments, that can be regions of surface transport convergence or barriers, leading to signatures in surface tracer fields that can be observed from space (SST, SSS, ocean color). Even though mapped altimetric geostrophic currents only resolve the larger Eulerian mesoscale field at scales  $> 150$  km, lagrangian techniques based on the temporal evolution of these gridded altimetric currents can generate horizontal stirring at the surface, and an energy cascade toward smaller-scale fronts and filaments.

Altimetric maps have been used to calculate the exponential rate of separation of particle trajectories, a basis for estimating eddy diffusivities and mixing rates from ocean space observations (e.g., Abernathey and Marshall 2013). Finite time or finite-size Lyapunov Exponents formalisms (FTLE Waugh and Abraham 2008; or FSLE, e.g., d’Ovidio et al. 2009) are useful indicators to delineate transport barriers that control the horizontal exchange of water in and out of eddy cores. Filaments generated by mesoscale stirring from altimetric currents have been shown to structure different phytoplankton communities (Abraham et al. 2000), and to impact on the repartition of higher trophic levels, up to top predators. Lagrangian stirring of large-scale surface salinity (SSS) fields by altimetric surface currents also shows promising results, for the reconstruction of finer scale SSS fronts in conditions where lateral advection dominates (Despres et al. 2011; Rogé et al. 2015).

Recent studies have also explored the mesoscale strain rate derived from gridded altimetric data, and its role in driving secondary ageostrophic vertical circulation around ocean dynamical fronts (e.g., Zhang et al. 2019; Balwada et al. 2021). The oceanic strain field is characterized by a local saddle point of geostrophic stream function, which stretches the flow along the front and compresses it across the front, thus enhancing the cross-frontal horizontal gradient (e.g., density gradient) (Klein and Lapeyre 2009). Composites constructed from Lagrangian surface drifters, satellite altimetry and satellite ocean color data show that when the mesoscale geostrophic strain rate is strong, it enhance the mesoscale fronts, but also drives the development of a secondary submesoscale ageostrophic circulation with strong vertical velocities, controlling nutrient upwelling and oceanic primary production (Zhang et al. 2019).

## 7.4 Two-dimensional Spectral Energy Fluxes

The ocean energy cascade from the deformation radius of the first baroclinic mode (10–100 km), toward larger scales, is called the “inverse cascade”, and there is also a “forward cascade” of energy down to smaller dissipation scales. The full 2D observed spectral energy fluxes can only be calculated from gridded altimetry maps (e.g., Scott and Wang 2005) and compared to models (see the review in Arbic et al. 2013). Modeling studies suggest that the inverse energy cascade between the large scales and the mesoscales is well represented by today’s altimetry maps (Arbic et al. 2013). Even though a “forward” energy cascade down to smaller dissipative scales has been estimated from spectral fluxes from altimetry (Scott and Wang 2005), it is more difficult to interpret whether they are physical, or an artifact of the smoothing inherent in the AVISO/CMEMS gridded altimeter products (Arbic et al. 2013). In the future, the 2D wide-swath observations from the SWOT mission should allow us to observe the finer details of the global variations of spectral kinetic energy fluxes with much less spatial smoothing.

## 7.5 Ocean Dynamical Regimes Revealed by Alongtrack Altimetric Wavenumber Spectra

The finest resolution of the mesoscale field available today is obtained with alongtrack altimeter data. Altimetric alongtrack sampling cannot track the movement of smaller individual eddies, but is ideal for calculating statistics of sea surface height wavenumber spectra, used to understand the underlying ocean dynamics leading to an energy cascade between the large-scale dynamics and the smallest observable scales. Over the mesoscale range that is observable with alongtrack altimetry (50–500 km), there is a steep decrease in power in the SSH spectra, from high power spectral density (PSD) levels near 500 km to low values at lower wavelengths. Altimetric SSH wavenumber spectra showing a power law of  $k^{-5}$ , where  $k$  is wavenumber, are consistent with ocean dynamics being governed by geostrophic turbulence, which has a  $k^{-3}$  velocity spectrum. Near the ocean surface, SSH can be governed by the surface quasi-geostrophic (SQG) dynamic regime and should follow  $k^{-11/3}$ , instead of  $k^{-5}$ . In low eddy energy regions, the presence of internal tides that are not in geostrophic balance can dominate over the SSH spectral cascade, and the alongtrack SSH wavenumber spectra exhibits flatter spectral slopes closer to  $k^{-1}$  or  $k^{-2}$ .

Long altimetric time series allow us to derive robust statistics on the regional variation of these wavenumber slopes, and on the underlying dynamical regimes. Xu and Fu (2012) produced estimates of the SSH wavenumber spectrum over the global oceans based on

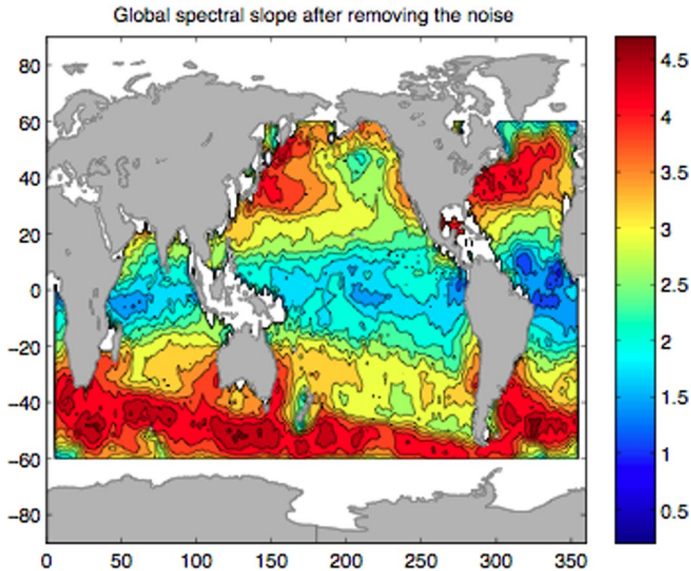


**Fig. 13** Global distribution of the spectral slopes of SSH wavenumber spectrum in the wavelength band of 70–250 km estimated from the Jason-1 altimeter measurements after removing the noise. The sign of the slopes was reversed to make the values positive (from Xu and Fu 2012)

7-years of Jason-1 data (Fig. 13), and identified distinct regional variations: Spectral slopes were only steeper than  $k^{-11/3}$ , approaching  $k^{-5}$ , in the core of the major current systems. The vast majority of the ocean interior poleward of  $20^\circ$  in latitude, had weaker SSH spectral slopes between  $k^{-11/3}$  and  $k^{-2}$ , and the SSH spectral slopes were flatter than  $k^{-2}$  within a narrow latitude band around the equator. Other studies showed that in the mid-latitudes, distinct seasonal variations occur in these altimetric SSH wavenumber spectral slopes, with steeper slopes occurring in the mesoscale range in summer when the EKE is strong, and flatter slopes in winter when the smaller-scale, deep-reaching mixed layer instabilities are most energetic (Callies and Ferrari 2013; Dufau et al. 2016; Vergara et al. 2019). The anisotropy of the ocean circulation has also been investigated globally from the difference in ascending and descending track altimetric wavenumber spectra (e.g., Wang et al. 2019b). These regionally varying dynamical regimes revealed by alongtrack altimetry have been confirmed, and their vertical structure explored, with in situ data (e.g., Callies and Ferrari 2013); and with ocean models.

One issue that has arisen over the last 10 years is the interaction of the internal tides with the mesoscale ocean circulation. This interaction generates non-phase-locked internal tide signals that occur over similar wavelengths to the mesoscale variability and can induce flatter wavenumber spectra and energy cascade in the tropics and in the low eddy energy eastern subtropical basins (Xu and Fu 2012; Dufau et al. 2016; Vergara et al. 2019). This is a major subject of research, since the mesoscale–internal tide interaction may be an important pathway to mixing and dissipation of the ocean circulation (see Sect. 9).

Today, the multi-decadal altimetric time series, combined with surface tracer information from satellite SST, SSS and ocean color data, have allowed a major increase in our understanding of the larger mesoscale ocean variability, its role in structuring the upper ocean's density gradients and biomass, and in the energy cascades to different scales. Yet,

the smallest mesoscales we can observe today with satellite altimetry are limited by the crosstrack altimetric spacing and the alongtrack noise levels (see Sect. 2), that block the observation of ocean dynamics at scales < 30–70 km, depending on the altimetric mission and technology (Vergara et al. 2019). With the future SWOT mission, we expect to observe finer scales in 2D, reaching 15–40 km depending on sea state (Wang et al. 2019a). Over the next decade, this combination of SWOT, multi-mission altimetry, and satellite tracer data, should allow us to better observe and extend our understanding of the smaller scales from 15–150 km, the missing link in today's ocean circulation from space.

## 8 Polar Ocean Circulation

Satellite radar altimetry is often presented as capable of observing the global ocean. Yet many global maps lack coverage in high-latitude areas. Large in situ experiments such as the MOSAiC cruise provide a wealth of observations over a limited time span but the polar oceans generally remain poorly observed by routine, long-term systems mainly due to harsh environmental conditions in these remote locations (Smith et al. 2019). Yet observing the polar regions is critical since the Arctic has warmed twice as fast as the global average (Cohen et al. 2014) and experienced dramatic sea ice decline. In this context, remote sensing in general and satellite radar altimetry in particular can provide valuable polar ocean observations: Latitudes up to 82° have been observed since 1991 (by the ERS, EnviSat, SARAL/AltiKa, and Sentinel-3 series), and CryoSat-2 provides observations up to 88° since 2010.

Observing the polar oceans remains a challenge for satellite altimetry: Sea ice cover prevents accurate measurements and almost all contributions to the final sea surface height estimation have higher error levels: altimeter range, geophysical corrections, mean sea surface models... Sea Surface Height (SSH) retrievals in ice-covered areas rely on the identification of leads (cracks) between ice floes (Quartly et al. 2019) that act as bright targets in the radar footprint. The corresponding echoes are specular (peaky waveforms) and must be processed using a specific retracking algorithm. Several groups have applied retracking algorithms in the sea ice zone, with slight variations in lead identification and retracking to produce estimates of Arctic SSH. Peacock and Laxon (2004) produced the first SSH variability map from ERS data. Their work was later updated with EnviSat data and used to estimate interannual freshwater storage variability in the Beaufort gyre (Giles et al. 2012), a prominent feature of the Arctic Ocean circulation. The inclusion of CryoSat-2 data (Armitage et al. 2016; Armitage et al. 2017) further extended the time span available for analysis and provided insights on seasonal geostrophic currents variability. Rose et al. (2019) processed the entire 1991–2018 period providing the longest available Arctic SSH dataset. Using this dataset, they are able to estimate the regional sea level trend (95% CI in [1.67; 2.54] mm/yr).

These reprocessed datasets are generally based on the analysis of one mission at a time and their resolution is therefore limited temporally (~one month) and spatially (~several 100 kms). Whereas the circulation in these polar regions is at much smaller scales (e.g., Newton et al. 1974) and higher resolution SSH products are required to address current oceanographic questions such as the Beaufort Gyre stability mechanisms (Doddridge et al. 2019). Higher resolution datasets have been released (Prandi et al. 2021) that leverage recent data processing advances with current altimeter constellation capabilities.

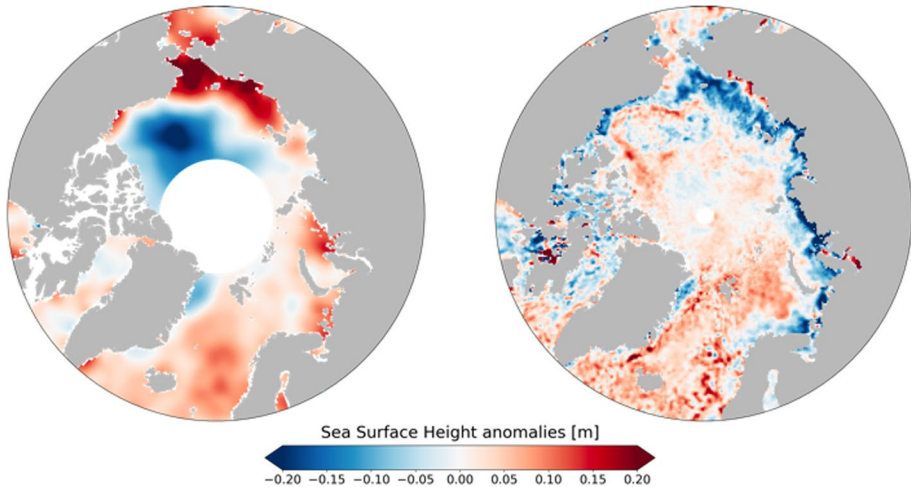


**Fig. 14** Maps of sea surface height anomalies (SSHA) in the Arctic Ocean from Armitage et al. 2016 data during September 2003 (left) and from Prandi et al. 2021 on September 12th 2017. SSHA fields are not directly comparable but illustrate the spatial resolution increase resulting from combining data from multiple altimeter missions

Recent physical retracking algorithms (Poisson et al. 2018; Tourain et al. 2021) rely on a model that can adapt to both diffuse (open ocean) and peaky (sea ice leads) echoes. Such adaptive retracers are more accurate than those using empirical algorithms and are able to consistently process the open ocean and ice-covered areas thus removing the need to estimate a bias between both surfaces. In recent years, up to 4 satellites have been providing data at latitudes greater than  $66^\circ$  (CryoSat-2, SARAL/AltiKa, Sentinel-3A and 3B), and combining these observations through optimal interpolation (Pascual et al. 2006) provides polar ocean fields with an unprecedented resolution. Typical sea level fields from a mono-mission product (from Armitage et al. 2016) and a multi-mission product (from Prandi et al. 2021) are shown on Fig. 14, from different periods since these products do not overlap in time. More small-scale structures are apparent, and comparisons to tide gauges show that the multi-mission dataset is also able to retrieve shorter period signals than a mono-mission dataset. This multi-mission dataset has revealed the existence of new circulation pathways north of Svalbard (Athanasé et al. 2021) thus demonstrating the ability of satellite altimetry to observe small-scale signals, even in ice-covered areas.

Although more studies have focused on the Arctic Ocean circulation, similar SSH datasets have been released over the Southern Ocean, and have been used to characterize the variability of the Antarctic Circumpolar Current and Antarctic Slope Current (Armitage et al. 2018), and the Ross Gyre (Dotto et al. 2018). A multi-mission altimetric dataset (Auger et al. 2022) has demonstrated its ability to capture small-scale variability of the slope current, consistent with wind forcing variability.

Polar ocean measurements still show higher error levels than global ocean products but the demonstrated impact of recent processing improvements, the generalization of delay-Doppler altimetry and the improved observation capabilities of current and future altimetry constellations will contribute to more accurate and higher resolution polar ocean sea level estimates.

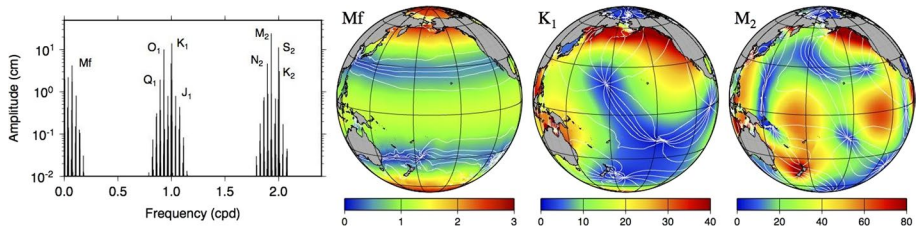


**Fig. 15** (Left) Spectrum of the tidal force expressed in terms of maximum height of equilibrium tide. Major lines are labeled according to Kelvin–Darwin conventions. (Right) Amplitudes (cm) in color and iso-phase lines in white of the largest long-period (Mf), diurnal (K<sub>1</sub>), and semi-diurnal (M<sub>2</sub>) tides. The diurnal and semi-diurnal tides are significantly larger than equilibrium. Tidal charts are from the FES2014 atlas (Lyard et al. 2021)

## 9 Tides and Internal Tides from Space

While tides are a fascinating branch of physical oceanography—they are the ocean’s response to a planetary scale force that is known almost perfectly—there has always been great practical motivation for the subject owing to many wide-ranging applications, from marine navigation and commercial shipping to satellite geodesy and oceanography. In many kinds of ocean measurements, tides are the dominating signal and must be removed before smaller, often subtle, signals of the ocean’s circulation and climate can be studied. For tide gauge measurements, removal of tidal signals requires only a well-designed digital filter. But for satellite measurements, in which an ocean location is visited only once every  $n$  days, the tidal signals are aliased to lower frequencies and, in fact, usually scattered throughout the spectrum. We must rely on tidal models to predict and remove these signals. A long-sought goal for the altimeter community has been to predict open ocean signals with an accuracy of 1 cm, and this goal is close to being achieved (Ray and Egbert 2017).

Satellite altimetry thus has a great need for accurate tidal “corrections,” but it also provides the most essential data for constructing the necessary models (Le Provost et al. 1995). The orbit of the Topex/Poseidon satellite was purposely designed to provide good tidal measurements, with dominant signals aliased to well-separated periods and away from major seasonal signals. (In contrast, Sun-synchronous altimeters provide little useful tidal information: Solar tides are observed always with the same phase, and other important waves are aliased to the annual cycle.) Within three years of the T/P launch, global tide models saw a dramatic improvement in accuracy (e.g., Shum et al. 1997), and now with almost three decades of data the models continue to be refined (Stammer et al. 2014), with even new details on the fine structure of the tidal spectrum being revealed (e.g., Ray 2020).

The tidal forced spectrum is indeed rich with structure (Fig. 15), simply because the orbit of the moon is quite complex (elliptical, inclined to the ecliptic and precessing, with large third-body effects from the sun). As Fig. 15 shows, the spatial patterns of the waves grow more complex with frequency. The long-period waves (e.g., Mf) are in near-equilibrium with the tidal potential, but ocean resonances in the diurnal and especially semi-diurnal bands lead to large amplitudes and distinctly non-equilibrium wave patterns.

One method used to map the global tide is purely empirical, treating altimeter data as simply a moving tide gauge that can be analyzed at the known tidal frequencies; a recent example is by Hart-Davis et al. (2021). A second approach is to employ data assimilation with a high-resolution numerical hydrodynamic model, which formally

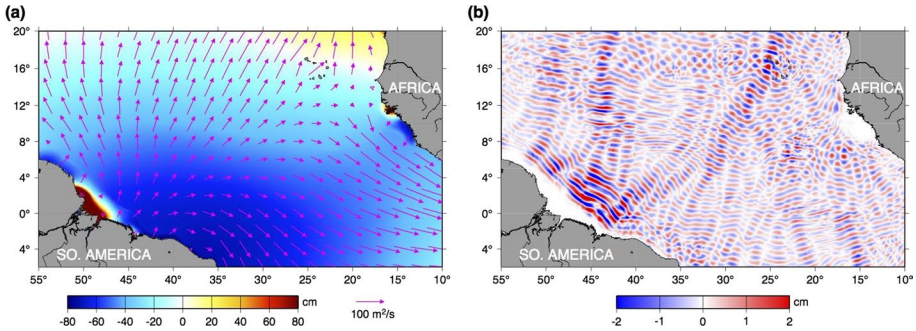


**Fig. 16** **a** Elevations (cm) of the  $M_2$  surface tide in the tropical Atlantic Ocean at the moment the Moon passes the Greenwich meridian. Elevations are evaluated from the FES2014 model (Lyard et al. 2021). Arrows denote tidal currents expressed in terms of volume transports (scale at bottom). **b** The  $M_2$  internal tide surface elevations (cm) when the Moon passes Greenwich. These are elevations coherent with the astronomical potential, taken from Zaron (2019)

incorporates both observations and dynamics and allows a tradeoff between the two based on error characteristics. The dynamics require accurate bathymetry and knowledge of dissipative processes. Examples based on tidal assimilation are the TPXO series of models (Egbert and Erofeeva 2002) and the FES series (Lyard et al. 2021). Empirical methods work exceedingly well in the open ocean, but even with three decades of altimetry in hand they are often found inadequate in shallower water, where wavelengths are much shorter, often shorter than the track spacing of repeated altimeter tracks (note the shallow water regions in Fig. 15, 16a). Empirical methods can benefit by adopting prior high-resolution models, and altimetry is then used (in a remove–restore procedure) to refine the prior (e.g., Hart-Davis et al. used the FES2014 model in their analysis). The shallow water mapping ultimately depends on the hydrodynamics and accurate bathymetry, and as altimetry is pushed ever more toward near-coastal waters, assimilation methods appear essential. (It is possible empirical approaches will make a comeback when several years of wide-swath altimetry are available.) Purely hydrodynamic models, typically needed as a prior for assimilation methods, have historically been far too inaccurate to be competitive with empirical or assimilation results, although they are now markedly improved. This is firstly due to the major efforts in collecting bathymetric measurements, building bathymetric databases and tools, and deriving bathymetric products that are more accurate and have a better representation of the smaller spatial scales. In addition, we now have computer resources with sufficiently high-resolution grids and—critically—improved knowledge obtained about tidal dissipation from altimeter analyses.

Shedding light on the long-standing problem of tidal energy dissipation (e.g., Munk 1997) was an early success of accurate tidal mapping with T/P altimetry. It had been thought since 1920 that most tidal dissipation occurs by boundary layer processes in shallow water, but the total appeared too low to match independent information (such as from the secular tidal acceleration of the moon). With altimeter maps setting tight constraints on dynamics, it became clear that significant dissipation was also occurring in the open ocean (Egbert and Ray 2000). This was realized to be the surface tide losing energy to internal tides and other baroclinic motions. Accounting for this energy conversion (Shakespeare et al. 2020) is a necessary step in improving hydrodynamic tide models.



When currents associated with the surface tide (Fig. 16a) impact undersea topography, internal waves of tidal frequency (i.e., internal tides) can be generated. The internal vertical displacements can be quite large, dozens of meters or more; the associated displacements at the surface are very small, a few cm or smaller, but these can be detected and now mapped with altimeters (Fig. 16b). Because the density contrasts within the water column are much smaller than at the air–water interface, the phase velocity of internal tides is much smaller than the surface tide, and the wavelengths are correspondingly short—of order 100 km, as in Fig. 16b. That satellite altimetry can map such small waves has opened up a new path in the study of internal tides (Zhao et al. 2012; Zaron 2019). The dissipation of these waves has possibly profound implications for ocean mixing (Munk 1997; Vic et al. 2019).

By the nature of how they are mapped, the internal tide signals, seen in Fig. 16b, are coherent (phase-locked) with the surface tide. Yet as the ocean stratification or the background (non-tidal) currents change, the generation as well as the propagation of internal tides must also change. For many years our picture of internal tides was one of waves highly incoherent in both space and time, sometimes even intermittent. That coherent waves as depicted in Fig. 16b even exist is somewhat surprising. It is likely, in fact, that Fig. 16b misses a large portion of internal waves that do not remain phase-locked and that are therefore much harder to map with an altimeter.

Mapping internal tides and understanding the degree that they remain stationary and phase-locked with the surface tide is an important topic of current research, with implications for all altimetry missions, including the future SWOT mission. The wavelengths in Fig. 16b fall within the mesoscale/submesoscale band that SWOT is designed to study. Unless SWOT is confined to measuring internal tides, these signals must be predicted and removed from the data, just like the surface tide must be predicted and removed from standard altimeter data. The prediction problem here, however, is far more challenging, and not only in terms of the short wavelengths that must be mapped. If a significant part of the internal tide variance is non-stationary and dependent on the ocean state, as seems possible and even likely, then the tidal problem becomes entangled with the problem of mapping the non-tidal variability. Studying the internal tides that are generated in high-resolution general circulation models that are forced by both the atmosphere and the tidal potential is helping clarify the problem and our understanding of the generation, propagation, and decay of internal tides (Arbic et al. 2018), and the comparison of the performance of several models (Carrere et al. 2021) in the end may be necessary to help with the prediction problem that is needed for high-resolution alongtrack and swath altimetry. The realism of these internal-tide models can be further improved by assimilating observations to correctly represent the mesoscale structures that interact with the tidal waves, and contribute to their non-phase-locked signals.

## 10 Assimilation in Ocean Circulation Models and Oceanic Reanalyses

Ocean data assimilation combines ocean observations and ocean models taking into account their respective errors to derive an optimal 4D estimation of the ocean state (e.g., see Moore et al. 2019 for a recent review). This is an essential step that transforms satellite and in situ observations into 4D ocean fields that are used to describe the state of the ocean in near real time (analyses) and to initialize ocean and coupled ocean/atmosphere models generating short term ocean forecasts and seasonal and long-term ocean/atmosphere forecasts.

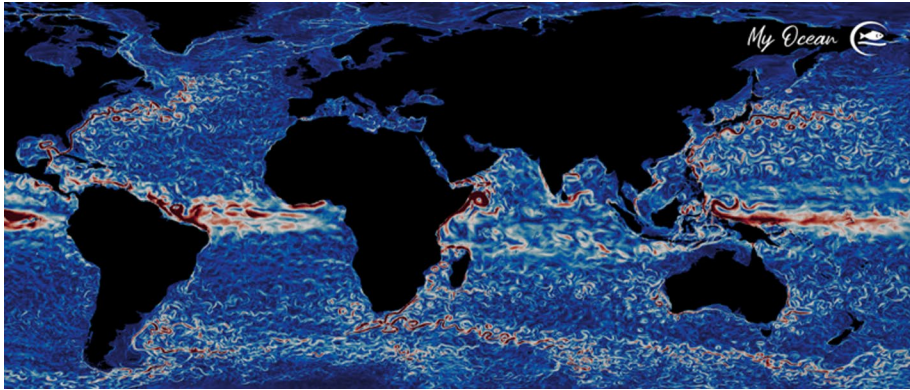


**Fig. 17** Surface currents 7-day forecasts for mid-August 2021 from the Mercator Ocean/Copernicus Marine Service global  $1/12^\circ$  data assimilation system. The system assimilates data from all available altimeter missions, satellite sea surface temperature data and a wide range of in situ observations (Argo, moorings, gliders, ships, and marine mammals)

Ocean data assimilation is also used to generate ocean reanalyses (e.g., Stammer et al. 2016; Storto et al. 2019; Lellouche et al. 2021) that provide consistent longtime series of the 4D ocean state (e.g., using the same model and same data assimilation system). The contribution of ocean reanalyses to the understanding of ocean dynamics has been demonstrated in numerous regional and global studies. Artana et al. (2019) have thus shown, for example, the major contributions of Mercator Ocean global ocean reanalyses to better understand variations in the Malvinas Current, the Brazil Current and in their confluence, a region with highly complex ocean dynamics.

Ocean modeling and data assimilation systems now operationally assimilate in situ and satellite data to provide regular and systematic reference information on the physical state (Fig. 17), variability, and dynamics of the ocean and marine biogeochemistry from global to coastal scales (e.g., Chassignet et al. 2018; Le Traon et al. 2019). Products serve a wide range of applications and downstream services (e.g., Bell et al. 2009, 2015; Le Traon et al. 2019). Modeling and data assimilation systems are a fundamental component of the value chain that goes from observations to applications and users (Le Traon et al. 2019).

There are a wide range of data assimilation techniques ranging from relatively simple schemes such as optimal interpolation or 3D-VAR, to more sophisticated ones, such as 4D-VAR, Kalman filters and smoothers and/or ensemble techniques (see Moore et al. 2019). The choice of a data assimilation scheme depends on the application and of the modeling and data assimilation system characteristics, in particular, the resolution and the associated computing cost.

Satellite altimetry is a critical observing system required for modeling and data assimilation (e.g., Le Traon et al. 2017). It provides global, real time, all-weather sea level measurements (SSH) with high space and time resolution. SSH is an integral of the ocean interior properties (SSH is related to depth-integrated density perturbations and barotropic motions) and is a strong constraint for inferring the 4D ocean circulation through data assimilation. Only altimetry can constrain, in particular, the 4D mesoscale circulation in ocean models which is required for most operational oceanography applications. High resolution from multiple altimeters is required to adequately represent ocean eddies and associated currents in models. Both Observing System Evaluations (OSEs) (e.g., Hamon

et al. 2019) and Observing System Simulation Experiments (OSSEs) (e.g., Verrier et al. 2017) demonstrate the major contribution of altimetry. At least four altimeters are required to constrain modeling and data assimilation systems. This is particularly true with high-resolution data assimilation systems. The new generation of nadir altimeters now provides enhanced capability, thanks to a Synthetic Aperture Radar (SAR) mode that reduces measurement noise. Verrier et al. (2018) demonstrated that the use of SAR multiple altimeter missions with high-resolution models will improve the capability of the ocean analysis and forecasting systems. A challenge in using nadir altimetry and future SWOT data for data assimilation is to estimate the data errors and characterize their space–time structures. Estimates are available for alongtrack altimetry (e.g., Taburet et al. 2019) and proposed for SWOT based on simulations (Chelton et al. 2019), but there is a need to continue research efforts on this issue.

Accurate knowledge of the Mean Dynamic Topography (MDT) is also a fundamental element for assimilation into ocean models. Thanks to new and improved altimetric, in situ and gravimetric (GRACE and GOCE satellite missions) data, MDTs are regularly updated, leading to considerable improvements in both forecasts and analyses. Hamon et al. (2019) showed, for example, that, in terms of the impact on reducing SSH errors, assimilating an updated release of the MDT is comparable to assimilating a fourth time-varying altimeter.

The role of satellite altimetry to ocean forecasting is essential but remains limited due to 1D nature of the sampling by nadir altimeters. Even with 3 to 4 altimeters, only wavelengths longer than 200 km can be adequately monitored. The development of wide-swath altimetry that will be demonstrated with the SWOT mission opens up very promising perspectives to improve our ability to monitor and forecast the smaller space and time scales (e.g., d’Addezio et al. 2019; Tchonang et al. 2021). Through a series of Observing System Simulation Experiments, Benkiran et al. (2021) and Tchonang et al. (2021) demonstrated that SWOT data could be readily assimilated in a global high resolution ( $1/12^\circ$ ) analysis and forecasting system with a positive impact everywhere and very good performances. Adding SWOT observations to those of three nadir altimeters globally reduced the variance of SSH and surface velocities analyses and forecasts by about 30% and 20%, respectively. The main limitation of SWOT is, however, related to its longtime repeat period. On the longer run, flying a constellation of two or three wide-swath altimeters would thus be highly beneficial to further improve the performances, in particular, for the small space and time scales.

## 11 Future Developments in Ocean Circulation from Space

Over the next decade, there are a number of key issues to ensure the continuity of the present observing system of ocean circulation from space, but also to extend and enhance our present capabilities. As this paper has discussed, the satellite-based ocean circulation observing system is largely constrained by multiple nadir altimeter missions, based on conventional or SAR technology. It is important that these altimetric missions continue to be maintained, and their orbits and space–time coverage be well coordinated to allow the optimal sampling of the ocean circulation as well as the continuity of the long-term time series. This continuity will be maintained by the European Sentinel-3 A-B and their extension with C-D, by the Sentinel-6A Michael Freilich and later with Sentinel-6B along the long-term Topex/Poseidon-Jason climate orbit, and will be completed by the Chinese/CNES HY-2 series. Other missions currently in flight complete this constellation (see Fig. 1).

A key aspect of the success of the altimetric monitoring of ocean circulation is due to the regular meetings and discussions between scientists and engineers within the international Ocean Surface Topography Science Team (OSTST). This annual forum allows for technical discussions on the data quality, external calibration and validation, inter-calibration between all altimetric missions, and scientific discussions on new results and applications. It is also a forum for programmatic discussions to help coordinate the data quality and sampling between different altimetric missions, and different space agencies. Individual altimetric missions have their own internal meetings, but the continuity of the international OSTST forum is critical for the precise data and good functioning of the entire altimetric constellation. Every 5 years, we also hold review meetings with the 15, 20 and 25 Years of Progress in Radar Altimetry Symposiums (e.g., <http://www.altimetry2018.org>).

Global and regional high-resolution models with enhanced space–time resolution and more complex dynamics will be widely available over the next decade (Fox-Kemper et al. 2019). Developing a satellite and in situ observing system with enhanced spatial and temporal resolution is key to accompany these models (see Sect. 10), and to understand and develop better parameterizations of the finer, rapidly evolving ocean dynamics. In a changing climate, it is critical to extend these observations into regions that have strong societal applications yet are poorly sampled today, including coastal and regional seas and the polar regions (Sect. 8).

A major revolution in our ocean circulation observing capabilities over the next few years will be wide-swath altimetry, with the arrival of the SWOT mission (see Sect. 4). These global observations over two 50 km wide swaths, with improved signal-to-noise, will allow us to observe the fine-scale ocean dynamics in 2D right up to the coast, extending into the estuaries, with greatly improved coverage in regional seas and in polar regions up to 78° in latitude. In addition to the 2 km resolution in 2-D SSH coverage, for the first time we will have fine-scale cross-swath gradients of sea surface height, to directly derive the 2D geostrophic velocity and vorticity/strain fields after removing the noise (see Sect. 7). These geostrophic vorticity and strain fields can be used to derive the finer-scale upper ocean 3D circulation, including vertical velocities below the mixed layer (Qiu et al. 2016) or the ageostrophic secondary circulation at fronts (e.g., Zhang et al. 2019). Full global coverage of daily SSH and geostrophic currents will still require interpolation of the multi-mission altimetry constellation including SWOT, or assimilation into ocean models (see Sect. 10). SWOT will fly for 3.5 years from early 2023 to late 2026, and other wide-swath altimeter missions may follow, including the Chinese Guanlan mission and the Sentinel-3 New Generation Topography mission from 2030 onwards.

SWOT's orbit has also been chosen to resolve the major ocean tide constituents, and after the 3.5 year mission, we expect a major improvement in coastal, regional and high-latitude barotropic tides, and a better observation of internal tides (see Sect. 9). This will allow improved tidal models ingesting SWOT data, leading to improved barotropic and coherent internal tide corrections for reprocessing of past altimetric missions, for predicting more accurate tide corrections for future missions, and tidal heights and currents for many coastal, regional and high-latitude applications.

A precise mean ocean circulation is required to calculate the ocean surface currents from the altimeter-derived ocean surface geostrophic current anomalies. We are expecting a major improvement in the mean sea surface products with the extended fine-scale coverage at 2 km resolution of SWOT, including in the coastal, regional, and polar seas. Once again, after 3-years of global coverage, SWOT should improve the mean sea surface and geoid models at short space scales, including the east–west gradients that are poorly sampled by alongtrack altimetry today (see Sect. 5). Improving the mean ocean

circulation not only requires having better Mean Sea Surface and geoid models, but also additional information about the ocean circulation from in situ measurements (drifting buoy velocities, HF radar,...) or from space (e.g., SAR Doppler velocities).

SWOT will cover the Antarctic seas, but extending and enhancing our observations into the Arctic Ocean also requires more polar-orbiting altimeters, since CryoSat and Saral/AltiKa are approaching their end of life. It is critical that future missions such as the bi-frequency Copernicus CRISTAL mission are launched soon (expected in 2027) to provide continuity and enhancement of our coverage of the polar oceans, and to better estimate the ocean circulation response to snow and sea ice variations in these rapidly evolving regions (Sect. 8).

This paper has concentrated on altimetric geostrophic currents that provide a strong constraint on our ocean state estimation (Sect. 10). However, today, total surface currents including the ageostrophic component of the ocean circulation cannot be observed directly from space, although the Ekman current component can be estimated from satellite scatterometer winds, the Stokes drift from wave models, and total surface currents can be derived from in situ data. The future may be with SAR Doppler surface velocity satellite missions: A number of propositions are being considered (e.g., OdySea–NASA/CNES, HARMONY—ESA, see Arduin et al. 2019 for a review) and airborne versions of the instrument are providing very good results. A future combination of SAR Doppler surface currents, combined with the depth-integrated geostrophic currents from swath and nadir altimetry, and polar-orbiting satellites, would better respond to our requirements for space observations of the ocean circulation.

**Funding** R.M. was supported by the French CNES TOSCA programs via SWOT project funding. L-L.F. was supported by the Jet Propulsion Laboratory, California Institute of Technology, under NASA SWOT Project funding. R.R. was supported by NASA Sentinel-6 and SWOT project funding.

## Declarations

**Conflict of interest** All authors declare that they have no conflict of interest.

**Open Access** This article is licensed under a Creative Commons Attribution 4.0 International License, which permits use, sharing, adaptation, distribution and reproduction in any medium or format, as long as you give appropriate credit to the original author(s) and the source, provide a link to the Creative Commons licence, and indicate if changes were made. The images or other third party material in this article are included in the article's Creative Commons licence, unless indicated otherwise in a credit line to the material. If material is not included in the article's Creative Commons licence and your intended use is not permitted by statutory regulation or exceeds the permitted use, you will need to obtain permission directly from the copyright holder. To view a copy of this licence, visit <http://creativecommons.org/licenses/by/4.0/>.

## References

- Abernathy RP, Marshall J (2013) Global surface eddy diffusivities derived from satellite altimetry. *J Geophys Res Oceans* 118:901–916. <https://doi.org/10.1002/jgrc.20066>
- Ablain M, Cazenave A, Larnicol G, Balmaseda M, Cipollini P, Faugère Y, Fernandes MJ, Henry O, Johannessen JA, Knudsen P, Andersen O, Legeais J, Meyssignac B, Picot N, Roca M, Rudenko S, Scharffenberg MG, Stammer D, Timms G, Benveniste J (2015) Improved sea level record over the satellite altimetry era (1993–2010) from the climate change initiative project. *Ocean Sci* 11:67–82. <https://doi.org/10.5194/os-11-67-2015>
- Abraham ER, Law CS, Boyd PW, Lavender SJ, Maldonado MT, Bowie A (2000) Importance of stirring in the development of an iron-fertilized phytoplankton bloom. *Nature* 407:727–730
- Andersen OB, Knudsen P, Stenseng, L (2015) The DTU13 MSS (mean sea surface) and MDT (mean dynamic topography) from 20 years of satellite altimetry. In: S Jin, R Barzaghi (Eds), *International*

- Association of Geodesy Symposia. Springer: Switzerland. pp. 1–10. doi [https://doi.org/10.1007/1345\\_2015\\_182](https://doi.org/10.1007/1345_2015_182)
- Arbic BK, Polzin KL, Scott RB, Richman JG, Shriver JF (2013) On eddy viscosity, energy cascades, and the horizontal resolution of gridded satellite altimeter products. *J Phys Oceanogr* 43(2):283–300. <https://doi.org/10.1175/JPO-D-11-0240.1>
- Arbic BK et al (2018) A primer on global internal tide and internal gravity wave continuum modeling in HYCOM and MITgcm. In: *New Frontiers in Operational Oceanography* E Chassignet, A Pascual, J Tintoré, J Verron Eds. GODAE Ocean View, 307–392, doi:<https://doi.org/10.17125/gov2018.ch13>.
- Ardhuin F, Chapron B, Maes C, Romeiser R, Gommenginger C, Cravatte S, Morrow R, Donlon C, Bourassa M (2019) Satellite doppler observations for the motions of the oceans. *B Am Meteorol Soc* 100:215–219. <https://doi.org/10.1175/BAMS-D-19-0039.1>
- Armitage TWK, Bacon S, Ridout AL, Thomas SF, Aksenov Y, Wingham DJ (2016) Arctic sea surface height variability and change from satellite radar altimetry and GRACE, 2003–2014. *Journal of Geophysical Research: Oceans* 121(6):4303–4322. <https://doi.org/10.1002/2015JC011579>
- Armitage T, Bacon S, Ridout A, Petty A, Wolbach S, Tsamados M (2017) Arctic ocean geostrophic circulation 2003–2014. *Arctic Ocean Geostroph Circulat*. <https://doi.org/10.5194/tc-2017-22>
- Armitage TWK, Kwok R, Thompson AF, Cunningham G (2018) Dynamic topography and sea level anomalies of the southern ocean: variability and teleconnections. *J Geophys Res Oceans* 123(1):613–630. <https://doi.org/10.1002/2017JC013534>
- Artana C, Provost C, Lellouche JM, Rio MH, Ferrari R, Sennéchaël N (2019) The malvinas current at the confluence with the brazil current: inferences from 25 years of mercator ocean reanalysis. *J Geophys Res Oceans* 124:7178–7200. <https://doi.org/10.1029/2019JC015289>
- Athanase M, Provost C, Artana C, Pérez-Hernández MD, Sennéchaël N, Bertosio C, Garric G, Lellouche JM, Prandi P (2021) Changes in atlantic water circulation patterns and volume transports north of Svalbard over the last 12 years (2008–2020). *J Geophys Res Oceans* 126(1):102. <https://doi.org/10.1029/2020JC016825>
- Auger M, Prandi P, Sallée JB (2022) Southern ocean sea level anomaly in the sea ice-covered sector from multimission satellite observations. *Sci Data* 9(1):70. <https://doi.org/10.1038/s41597-022-01166-z>
- Ballarotta M, Ubelmann C, Pujol MI, Taburet G, Fournier F, Legeais JF, Faugère Y, Delepouille A, Chelton D, Dibarboure G, Picot N (2019) On the resolutions of ocean altimetry maps. *Ocean Sci* 15:1091–1109. <https://doi.org/10.5194/os-15-1091-2019>
- Balwada D, Xiao Q, Smith S, Abernathy R, Gray AR (2021) Vertical fluxes conditioned on vorticity and strain reveal submesoscale ventilation. *J Phys Oceanogr* 51(9):2883–2901. <https://doi.org/10.1175/JPO-D-21-0016.1>
- Bell MJ, Lefebvre M, Le Traon PY, Smith N, Wilmer-Becker K (2009) The global ocean data assimilation experiment. *Oceanography* 22(3):14–21
- Bell MJ, Schiller A, Le Traon PY, Smith NR, Dombrowsky E, Wilmer-Becker K (2015) An introduction to GODAE ocean view. *J Operat Oceanogr* 8(1):s2–s11. <https://doi.org/10.1080/1755876X.2015.1022041>
- Benkiran M, Ruggiero G, Greiner E, Le Traon PY, Rémy E, Lellouche JM, Bourdallé-Badie R, Drillet Y, Tchoung B (2021) Assessing the impact of the assimilation of SWOT observations in a global high-resolution analysis and forecasting system part 1: methods. *Front Mar Sci* 8:691955. <https://doi.org/10.3389/fmars.2021.691955>
- Boy F, Desjonquères JD, Picot N, Moreau T, Raynal M (2017) CryoSat-2 SAR mode over oceans: processing methods, global assessment and benefits. *IEEE Trans Geosci Remote Sens* 55:148–158. <https://doi.org/10.1109/TGRS.2016.2601958>
- Brown G (1977) The average impulse response of a rough surface and its applications. *IEEE J Oceanic Eng* 2(1):67–74. <https://doi.org/10.1109/JOE.1977.1145328>
- Caballero A, Mulet S, Ayoub N, Manso-Narvarte I, Davila X, Boone C, Toublanc F, Rubio A (2020) Integration of HF radar observations for an enhanced coastal mean dynamic topography. *Front Mar Sci* 7:13. <https://doi.org/10.3389/fmars.2020.588713>
- Cai W, Borlace S, Lengaigne M, van Rensch P, Collins M, Vecchi G, Timmermann A, Santoso A, McPhaden MJ, Wu L, England MH, Wang G, Guilyardi E, Jin FF (2014) Increasing frequency of extreme El Niño events due to greenhouse warming. *Nat Clim Chang* 4(2):111–116. <https://doi.org/10.1038/nclimate2100>
- Callies J, Ferrari R (2013) Interpreting energy and tracer spectra of upper-ocean turbulence in the sub-mesoscale range (1–200 km). *J Phys Oceanogr* 43(11):2456–2474. <https://doi.org/10.1175/JPO-D-13-063.1>
- Capotondi A, Wittenberg AT, Newman M, di Lorenzo E, Yu JY, Braconnot P, Cole J, Dewitte B, Giese B, Guilyardi E, Jin FF, Karnauskas K, Kirtman B, Lee T, Schneider N, Xue Y, Yeh SW (2015)

- Understanding ENSO diversity. *Bull Am Meteor Soc* 96(6):921–938. <https://doi.org/10.1175/BAMS-D-13-00117.1>
- Carrere L, Arbic BK, Dushaw B, Egbert G, Erofeeva S, Lyard F, Ray RD, Ubelmann C, Zaron E, Zhao Z, Shriver JF, Buijsman MC, Picot N (2021) Accuracy assessment of global internal-tide models using satellite altimetry. *Ocean Sci* 17:147–180. <https://doi.org/10.5194/os-17-147-2021>
- Chafik L, Nilsen JEØ, Dangendorf S et al (2019) North atlantic ocean circulation and decadal sea level change during the altimetry era. *Nat Sci Rep* 9:1041. <https://doi.org/10.1038/s41598-018-37603-6>
- Chassignet EP, Pascual A, Tintoré J, Verron J (2018) New frontiers in operational oceanography. *GODAE Ocean View* 102:815. <https://doi.org/10.17125/gov2018>
- Chelton DB, Xie SP (2010) Coupled ocean-atmosphere interaction at oceanic mesoscales. *Oceanogr* 23:52–69
- Chelton DB, deSzoek RA, Schlax MG, El Naggar K, Siwertz N (1998) Geographical variability of the first baroclinic rossby radius of deformation. *J Phys Oceanogr* 28(3):433–460. [https://doi.org/10.1175/1520-0485\(1998\)028%3c0433:GVOTFB%3e2.0.CO;2](https://doi.org/10.1175/1520-0485(1998)028%3c0433:GVOTFB%3e2.0.CO;2)
- Chelton DB, Ries JC, Haines BJ, Fu LL, Callahan PS (2001). In: Fu LL, Cazenave A (eds) *Satellite altimetry and Earth sciences: a handbook of techniques and applications*. Academic Press, San Diego, pp 1–131
- Chelton DB, Schlax MG, Samelson RM, de Szoek RA (2007) Global observations of large oceanic eddies. *Geophys Res Lett* 34:L15606. <https://doi.org/10.1029/2007GL030812>
- Chelton DB, Schlax MG, Samelson RM (2011) Global observations of nonlinear mesoscale eddies. *Prog Oceanogr* 91:167–216. <https://doi.org/10.1016/j.pocean.2011.01.002>
- Chelton DB, Schlax MG, Samelson RM, Farrar JT, Molemaker MJ, McWilliams JC, Gula J (2019) Prospects for future satellite estimation of small-scale variability of ocean surface velocity and vorticity. *Prog Oceanogr* 173(2019):256–350. <https://doi.org/10.1016/j.pocean.2018.10.012>
- Chen G, Tang J, Zhao C, Wu S, Yu F, Ma C, Xu Y, Chen W, Zhang Y, Liu J, Wu L (2019) Concept design of the “guanlan” science mission: china’s novel contribution to space oceanography. *Front Mar Sci* 6:194. <https://doi.org/10.3389/fmars.2019.00194>
- Cheney RE, Marsh JG, Beckley BD (1983) Global me- soscale variability from repeat tracks of SEASAT altimeter data. *J Geophys Res* 88:4343–4354. <https://doi.org/10.1029/JC088iC07p04343>
- Cohen J, Screen JA, Furtado JC, Barlow M, Whittleston D, Coumou D, Francis J et al (2014) Recent arctic amplification and extreme mid-latitude weather. *Nat Geosci* 7(9):627–37. <https://doi.org/10.1038/ngeo2234>
- D’Addezio JM, Smith S, Jacobs GA, Helber RW, Rowley C, Souopgui I et al (2019) Quantifying wavelengths constrained by simulated SWOT observations in a submesoscale resolving ocean analysis/forecasting system. *Ocean Model* 135:40–55. <https://doi.org/10.1016/j.ocemod.2019.02.001>
- d’Ovidio F, Isern-Fontanet J, López C, Hernández-García E, García-Ladona E (2009) Comparison between Eulerian diagnostics and finite-size Lyapunov exponents computed from altimetry in the Algerian basin. *Deep Sea Res, Part I* 56(1):15–31
- Desprès A, Reverdin G, D’ Ovidio F (2011) Mechanisms and spatial variability of meso scale frontogenesis in the northwestern subpolar gyre. *Ocean Model* 39:97–113. <https://doi.org/10.1016/j.ocemod.2010.12.005>
- Dibarboure G, Boy F, Desjonqueres JD, Labroue S, Lasne Y, Picot N, Poisson JC, Thibaut P (2014) Investigating short wavelength correlated errors on low-resolution mode altimetry. *J Atmos Ocean Technol* 31:1337. <https://doi.org/10.1175/JTECH-D-13-00081>
- Doddridge EW, Meneghello G, Marshall J, Scott J, Lique C (2019) A three-way balance in the beaufort gyre: the ice-ocean governor, wind stress, and eddy diffusivity. *J Geophys Res Oceans* 124(5):3107–3124. <https://doi.org/10.1029/2018JC014897>
- Dong C, McWilliams JC, Liu Y, Chen D (2014) Global heat and salt transports by eddy movement. *Nat Commun*. <https://doi.org/10.1038/ncomms4294>
- Dotto TS, Naveira Garabato A, Bacon S, Tsamados M, Holland PR, Hooley J, Frajka-Williams E, Ridout A, Meredith MP (2018) Variability of the ross gyre, southern ocean: drivers and responses revealed by satellite altimetry. *Geophys Res Lett* 45(12):6195–6204. <https://doi.org/10.1029/2018GL078607>
- Dufau C, Orszynowicz M, Dibarboure G, Morrow R, Le Traon PY (2016) Mesoscale resolution capability of altimetry: present & future. *J Geophys Res Oceans* 121:4910–4927. <https://doi.org/10.1002/2015JC010904>
- Egbert GD, Erofeeva SY (2002) Efficient inverse modeling of barotropic ocean tides. *J Atmos Oceanic Tech* 19:183–204
- Egbert GD, Ray RD (2000) Significant dissipation of tidal energy in the deep ocean inferred from satellite altimeter data. *Nature* 405:775–778. <https://doi.org/10.1038/35015531>

- Egido A, Smith WHF (2017) Fully focused SAR altimetry: theory and applications. *IEEE Trans Geosci Remote Sens* 55:1. <https://doi.org/10.1109/TGRS.2016.2607122>
- Faghmous J, Frenger I, Yao Y et al (2015) A daily global mesoscale ocean eddy dataset from satellite altimetry. *Sci Data* 2:150028. <https://doi.org/10.1038/sdata.2015.28>
- Farrar JT (2011) Barotropic rossby waves radiating from tropical instability waves in the Pacific Ocean. *J Phys Oceanogr* 41:1160–1181. <https://doi.org/10.1175/2011JPO4547.1>
- Farrar JT, Durland TS (2012) Wavenumber-frequency spectra of inertia-gravity and mixed rossby-gravity waves in the equatorial Pacific Ocean. *J Phys Oceanogr* 42:1859–1881
- Farrar JT, Durland T, Jayne SR, Price JF (2021) Long-distance radiation of rossby waves from the equatorial current system. *J Phys Oceanogr* 51(6):1947–1966. <https://doi.org/10.1175/JPO-D-20-0048.1>
- Fox-Kemper B, Adcroft A, Böning CW, Chassignet EP, Curchitser E, Danabasoglu G, Eden C, England MH, Gerdes R, Greatbatch RJ, Griffies SM, Hallberg RW, Hanert E, Heimbach P, Hewitt HT, Hill CN, Komuro Y, Legg S, Le Sommer J, Masina S, Marsland SJ, Penny SG, Qiao F, Ringler TD, Treguier AM, Tsujino H, Uotila P, Yeager SG (2019) Challenges and prospects in ocean circulation models. *Front Mar Sci*. <https://doi.org/10.3389/fmars.2019.00065>
- Frajka-Williams E (2019) Atlantic meridional overturning circulation: observed transport and variability. *Front Mar Sci*. <https://doi.org/10.3389/fmars.2019.00260>
- Frappart F, Blumstein D, Cazenave A, Ramillien G, Birol F, Morrow R, Rémy F (2017) Satellite altimetry: principle and major applications in Earth Sciences. In: Webster J (ed) *Wiley encyclopedia of electrical and electronics engineering*. Wiley, New Jersey, pp 1–25
- Frenger I, Münnich M, Gruber N, Knutti R (2015) Southern ocean eddy phenomenology. *J Geophys Res Oceans* 120:7413–7449. <https://doi.org/10.1002/2015JC011047>
- Fu LL, Chelton DB (2001) Large-scale ocean circulation. In: Fu L-L, Cazenave A (eds) *Satellite altimetry and earth sciences: a handbook for techniques and applications*. Academic Press, New Jersey, pp 133–169
- Fu LL, Rodriguez ER (2004) High-resolution measurement of ocean surface topography by radar interferometry for oceanographic and geophysical applications. *AGU Geophys Monogr* 19:209–224
- Fu LL, Rodriguez E, Alsdorf D, Morrow R (eds) (2012) *The SWOT mission science document*. JPL publication. [https://swot.jpl.nasa.gov/files/swot/SWOT\\_MSD\\_1202012.pdf](https://swot.jpl.nasa.gov/files/swot/SWOT_MSD_1202012.pdf)
- Fu LL, Ubelmann C (2014) On the transition from profile altimeter to swath altimeter for observing global ocean surface topography. *J Atmos Ocean Technol* 31:560–568. <https://doi.org/10.1175/JTECH-D-13-00109.1>
- Fu L, Chelton DB, Le Traon PY, Morrow R (2010) Eddy dynamics from satellite altimetry. *Oceanogr Magaz* 23:4
- Fu LL, Lee T, Liu WT, Kwok R (2019) Fifty years of satellite remote sensing of the ocean. In: a century of progress in atmospheric and related sciences: celebrating the American meteorological society centennial. *Meteor Monogr*. <https://doi.org/10.1175/AMSMONOGRAPHS-D-18-0010.1>
- Gaube P, Chelton DB, Samelson RM, Schlax MG, O’Neill LW (2015) Satellite observations of mesoscale eddy-induced Ekman pumping. *J Phys Oceanogr* 45:104–132
- Giles KA, Laxon SW, Ridout AL, Wingham DJ, Bacon S (2012) Western arctic ocean freshwater storage increased by wind-driven spin-up of the beaufort gyre. *Nat Geosci* 5(3):194–197. <https://doi.org/10.1038/ngeo1379>
- Gourcuff C, Lherminier P, Mercier H, Le Traon P-Y (2011) Altimetry combined with hydrography for ocean transport estimation. *J Atmos Ocean Technol* 28(10):1324–1337. <https://doi.org/10.1175/2011JTECH0818.1>
- Hamlington BD, Strassburg MW, Leben RR, Han W, Nerem RS, Kim KY (2014) Uncovering an anthropogenic sea-level rise signal in the Pacific Ocean. *Nat Clim Chang* 4:782–785. <https://doi.org/10.1038/nclimate2307>
- Hamon M, Greiner E, Le Traon P, Remy E (2019) Impact of multiple altimeter data and mean dynamic topography in a global analysis and forecasting system. *J Atmos Oceanic Tech* 36(7):1255–1266. <https://doi.org/10.1175/JTECH-D-18-0236.1>
- Hart-Davis MG, Piccioni G, Dettmering D, Schwatke C, Passaro M, Seitz F (2021) EOT20: a global ocean tide model from multi-mission satellite altimetry. *Earth Syst Sci Data*. <https://doi.org/10.5194/essd-2021-97>
- Kelly KA, Willis JK, Reverdin G, Dong S, Thompson L (2017) Monitoring and interpreting mid-latitude oceans by satellite altimetry. In: *satellite altimetry over oceans and land surfaces*. CRC Press: New York, pp 102
- Klein P, Lapeyre G (2009) The oceanic vertical pump induced by mesoscale and submesoscale turbulence. *Annu Rev Mar Sci* 1:351–375



- Laignel B, Vignudelli S, Almar R, Becker M, Bentamy A, Benveniste J, Birol F, Frappart F, Idier D, Salameh E, Passaro M, Menendez M, Simard M, Turki I, Verpoorter C (2022) Observation of the coastal areas, estuaries and deltas from space. *Surveys Geophys.* 10:102. <https://doi.org/10.1007/s10712-022-09757-6>
- Le Provost C, Bennett AF, Cartwright DE (1995) Ocean tides for and from topex/poseidon. *Science* 267:639–642
- Le Traon PY et al (2019) From observation to information and users: the copernicus marine service perspective. *Front Mar Sci* 6(234):22. <https://doi.org/10.3389/fmars.2019.00234>
- Leben RR, Hamlington BD, Haines BJ (2011) Seasat and geosat revisited: using sea level measurements to improve satellite altimeter orbits. *J Astronaut Sci* 58:479–493
- Legeckis R (1977) Long waves in the eastern equatorial pacific ocean: a view from a geostationary satellite. *Science* 197:1179–1181. <https://doi.org/10.1126/science.197.4309.1179>
- Lellouche JM, Greiner E, Bourdallé-Badie R, Garric G, Melet A, Drevillon M, Bricaud M Hamon, Le Galoudec O, Regnier C, Candela T, Testut CE, Gasparin F, Ruggiero G, Benkiran M, Drillet Y, Le Traon PY (2021) The copernicus global 1/12° oceanic and sea ice GLORYS12 reanalysis. *Front Earth Sci* 9:698876. <https://doi.org/10.3389/feart.2021.698876>
- Levitus S, Antonov JI, Boyer TP, Locarnini RA, Garcia HE, Mishonov AV (2009) Global ocean heat content 1955–2008 in light of recently revealed instrumentation problems. *Geophys Res Lett* 36:07608. <https://doi.org/10.1029/2008GL037155>
- Levy M, Ferrari R, Franks PJP, Martin AP, Riviere P (2012) Bringing physics to life at the submesoscale. *Geophys Res Lett* 39:L14602. <https://doi.org/10.1029/2012GL052756>
- Llovel W, Penduff T, Meyssignac B, Molines JM, Terray L, Bessières L, Barnier B (2018) Contributions of atmospheric forcing and chaotic ocean variability to regional sea level trends over 1993–2015. *Geophys Res Lett* 45(13):405–413. <https://doi.org/10.1029/2018GL080838>
- Lyard F, Allain D, Cancet M, Carrère L, Picot N (2021) FES2014 global ocean tide atlas: design and performance. *Ocean Sci* 17:615–649. <https://doi.org/10.5194/os-17-615-2021>
- Lyman JM, Chelton DB, de Szoeke RA, Samelson RM (2005) Tropical instability waves as a resonance between equatorial rossby waves. *J Phys Oceanogr* 35:232–254. <https://doi.org/10.1175/JPO-2668.1>
- Martínez-Moreno J, Hogg AM, England MH et al (2021) Global changes in oceanic mesoscale currents over the satellite altimetry record. *Nat Clim Chang* 11:397–403. <https://doi.org/10.1038/s41558-021-01006-9>
- Maximenko NA, Niiler PP (2005) Hybrid decade-mean global sea level with mesoscale resolution. In: Saxena N (ed) Recent advances in marine science and technology. PACON International, Honolulu, pp 55–59
- McCarthy GD, Brown PJ, Flagg CN, Goni G, Houpert L, Hughes CW et al (2020) Sustainable observations of the AMOC: methodology and technology. *Rev Geophys* 58:e2019RG000654. <https://doi.org/10.1029/2019RG000654>
- Mercier H, Lherminier P, Sarafanov A, Gaillard F, Daniault N, Desbroyères D, Falina A, Ferron B, Gourcuff C, Huck T, Thierry V (2015) Variability of the meridional overturning circulation at the Greenland-Portugal OVIDE section from 1993 to 2010. *Prog Oceanogr* 132:250–261. <https://doi.org/10.1016/j.pocean.2013.11.001>
- Moore AM, Martin MJ, Akella S, Arango HG, Balmaseda M, Bertino L, Ciavatta S, Cornuelle B, Cummings J, Frolov S, Lermusiaux P, Oddo P, Oke PR, Storto A, Teruzzi A, Vidard A, Weaver AT (2019) Synthesis of ocean observations using data assimilation for operational, real-time and reanalysis systems: a more complete picture of the state of the ocean. *Front Mar Sci* 6:90. <https://doi.org/10.3389/fmars.2019.00090>
- Morrow R, Le Traon PY (2012) Recent advances in observing mesoscale ocean dynamics with satellite altimetry. *Adv Space Res* 50(8):1062–1076. <https://doi.org/10.1016/j.asr.2011.09.033>
- Morrow R, Blumstein D, Dibarboure G (2018) Finescale altimetry and the future SWOT mission. In: New frontiers in operational oceanography GODAE ocean view international school special edition. pp 815. <https://doi.org/10.17125/gov2018>
- Morrow R, Fu LL, Arduin F, Benkiran M, Chapron B, Cosme E, d’Ovidio F, Farrar JT, Gille ST, Lapeyre G, Le Traon P-Y, Pascual A, Ponte A, Qiu B, Rasclé N, Ubelmann C, Wang J, Zaron E (2019) Global observations of fine-scale ocean surface topography with the surface water and ocean topography (SWOT) mission. *Front Mar Sci.* <https://doi.org/10.3389/fmars.2019.0023>
- Mulet S, Rio MH, Mignot A, Guinehut S, Morrow R (2012) A new estimate of the global 3D geostrophic ocean circulation based on satellite data and in-situ measurements. *Deep Sea Res Part II* 77–80:70–81. <https://doi.org/10.1016/j.dsr2.2012.04.012>

- Mulet S, Rio MH, Etienne H, Artana C, Cancet M, Dibarboure G, Feng H, Husson R, Picot N, Provost C, Strub PT (2021) The new CNES-CLS18 global mean dynamic topography. *Ocean Sci* 17:789–808. <https://doi.org/10.5194/os-17-789-2021>
- Munk W (1997) Once again—tidal friction. *Prog Oceanogr* 40:7–35
- Newton JL, Aagaard K, Coachman LK (1974) Baroclinic eddies in the arctic ocean. *Deep-Sea Res Oceanogr Abstr* 21(9):707–719. [https://doi.org/10.1016/0011-7471\(74\)90078-3](https://doi.org/10.1016/0011-7471(74)90078-3)
- Pascual A, Faugère Y, Larnicol G, Le Traon PY (2006) Improved description of the ocean mesoscale variability by combining four satellite altimeters. *Geophys Res Lett.* <https://doi.org/10.1029/2005GL024633>
- Pavlis NK, Holmes SA, Kenyon SC, Factor JK (2012) The development and evaluation of the earth gravitational model 2008 (EGM2008). *J Geophys Res* 117:B04406. <https://doi.org/10.1029/2011JB008916>
- Peacock NR, Laxon SW (2004) Sea Surface Height Determination in the Arctic Ocean from ERS Altimetry. *J Geophys Res* 109(C7):C07001. <https://doi.org/10.1029/2001JC001026>
- Pegliasco C, Chaigneau A, Morrow R, Dumas F (2021) Detection and tracking of mesoscale eddies in the mediterranean sea: a comparison between the sea level anomaly and the absolute dynamic topography fields. *Adv Space Res* 68:401–419. <https://doi.org/10.1016/j.asr.2020.03.039>
- Penduff T, Juza M, Barnier B, Zika J, Dewar WK, Treguier AM et al (2011) Sea-level expression of intrinsic and forced ocean variabilities at interannual time scales. *J Clim* 24(21):5652–5670. <https://doi.org/10.1175/JCLI-D-11-00077>
- Poisson JC, Quartly GD, Kurekin AA, Thibaut P, Hoang D, Nencioli F (2018) Development of an ENVISAT altimetry processor providing sea level continuity between open ocean and arctic leads. *IEEE Trans Geosci Remote Sens* 56(9):5299–5319. <https://doi.org/10.1109/TGRS.2018.2813061>
- Prandi P, Poisson JC, Faugère Y, Guillot A, Dibarboure G (2021) Arctic sea surface height maps from multi-altimeter combination. *Earth Syst Sci Data Discuss.* <https://doi.org/10.5194/ESSD-2021-123>
- Pujol M-I, Faugère Y, Taburet G, Dupuy S, Pelloquin C, Ablain M, Picot N (2016) DUACS DT2014: the new multi-mission altimeter data set reprocessed over 20 years. *Ocean Sci* 12:1067–1090. <https://doi.org/10.5194/os-12-1067-2016>
- Pujol MI, Schaeffer P, Faugere Y, Raynal M, Dibarboure G, Picot N (2018) Gauging the improvement of recent mean sea surface models: A new approach for identifying and quantifying their errors. *J Geophys Res Oceans* 123:1056. <https://doi.org/10.1029/2017JC013503>
- Qiu B, Chen S (2005) Variability of the kuroshio extension jet, recirculation gyre, and mesoscale eddies on decadal time scales. *J Phys Oceanogr* 35(11):2090–2103. <https://doi.org/10.1175/JPO2807.1>
- Qiu B, Chen S (2011) Effect of decadal Kuroshio Extension jet and eddy variability on the modification of North Pacific in-termediate water. *J Phys Oceanogr* 41:503–515. <https://doi.org/10.1175/2010JPO4575.1>
- Qiu B, Chen S, Klein P, Sasaki H, Sasai Y (2014) Seasonal mesoscale and submesoscale eddy variability along the North Pacific subtropical counter current. *J Phys Oceanogr* 44:3079–3098. <https://doi.org/10.1175/JPO-D-14-0071.1>
- Qiu B, Chen S, Klein P, Ubelmann C, Fu L-L, Sasaki H (2016) Reconstructability of 3-dimensional upper ocean circulation from SWOT sea surface height measurements. *J Phys Oceanogr* 46:947–963
- Quartly GD, Srokosz MA, McMillan AC (2001) Analyzing altimeter artifacts: statistical properties of ocean waveforms. *J Atmos Ocean Tech* 18(12):2074–2091
- Quartly GD, Rinne E, Passaro M, Andersen OB, Dinardo S, Fleury S, Guillot A et al (2019) Retrieving sea level and freeboard in the arctic: a review of current radar altimetry methodologies and future perspectives. *Remote Sens.* <https://doi.org/10.3390/RS11070881>
- Raney RK (1998) The delay/doppler radar altimeter. *IEEE Trans Geosci Remote Sens* 36(5):1578–1588. <https://doi.org/10.1109/36.718861>
- Ray RD (2020) First global observations of third-degree ocean tides. *Sci Adv* 6:4744. <https://doi.org/10.1126/sciadv.abd4744>
- Ray RD, Egbert GD (2017) Tides and satellite altimetry. In: Stammer D, Cazenave A (eds) *Satellite altimetry over oceans and land surfaces*. CRC Press, New York, pp 427–458
- Ray RD, Zaron ED (2016) M2 internal tides and their observed wavenumber spectra from satellite altimetry. *J Phys Oceanogr* 46(1):3–22. <https://doi.org/10.1175/JPO-D-15-0065.1>
- Richman JG, Arbic BK, Shriver JF, Metzger EJ, Wallcraft AJ (2012) Inferring dynamics from the wavenumber spectra of an eddying global ocean model with embedded tides. *J Geophys Res* 117:C12012. <https://doi.org/10.1029/2012JC008364>
- Rieck JK, Böning CW, Greatbatch RJ, Scheinert M (2015) Seasonal variability of eddy kinetic energy in a global high-resolution ocean model. *Geophys Res Lett* 42:9379–9386. <https://doi.org/10.1002/2015GL066152>

- Rieu P, Moreau T, Cadier E, Raynal M, Clerc S, Donlon C, Borde F, Boy F, Maraldi C (2021) Exploiting the Sentinel-3 tandem phase dataset and azimuth oversampling to better characterize the sensitivity of SAR altimeter sea surface height to long ocean waves. *Adv Space Res* 67:253–265. <https://doi.org/10.1016/j.asr.2020.09.037>
- Rio MH, Hernandez F (2004) A mean dynamic Topography computed over the world ocean from altimetry, in-situ measurements and a geoid mod-el. *J Geophys Res* 109:12
- Rodriguez E, Fernandez DE, Peral E, Chen CW, De Bleser JW, Williams B (2017) Wide-swath altimetry: a review. In: Stammer D, Cazenave A (eds) *Satellite altimetry over oceans and land surfaces*. CRC Press, New York, pp 71–112
- Roemmich D, Johnson GC, Riser S, Davis R, Gilson J, Owens WB, Garzoli SL, Schmid C, Ignaszewski M (2009) The argo program: observing the global ocean with profiling floats. *Oceanography* 22(2):34–43. <https://doi.org/10.5670/oceanog.2009.36>
- Roessler A, Rhein M, Kieke D, Mertens C (2015) Long-term observations of North Atlantic Current transport at the gateway between western and eastern Atlantic. *J Geophys Res C: Oceans*. <https://doi.org/10.1002/2014JC010662>
- Rogé M, Morrow R, Dencausse G (2015) Altimetric lagrangian advection to reconstruct Pacific Ocean fine scale surface tracer fields. *Ocean Dyn* 65:1249–1268. <https://doi.org/10.1007/s10236-015-0872-4>
- Rose SK, Andersen OB, Passaro M, Ludwigsen CA, Schwatke C (2019) Arctic ocean sea level record from the complete radar altimetry Era: 1991–2018. *Remote Sens* 11(14):16. <https://doi.org/10.3390/rs1141672>
- Sandwell DT, Smith WHF (2009) Global marine gravity from retracked Geosat and ERS-1 altimetry: Ridge segmentation versus spreading rate. *J Geophys Res* 114:B01411. <https://doi.org/10.1029/2008JB006008>
- Sasaki H, Klein P, Qiu B et al (2014) Impact of oceanic-scale interactions on the seasonal modulation of ocean dynamics by the atmosphere. *Nat Commun* 5:5636. <https://doi.org/10.1038/ncomms6636>
- Scharffenberg MG, Stammer D (2010) Seasonal variations of the large-scale geostrophic flow field and eddy kinetic energy inferred from the TOPEX/Poseidon and Jason-1 tandem mission data. *J Geophys Res* 115:C02008. <https://doi.org/10.1029/2008JC005242>
- Schmid C (2014) Mean vertical and horizontal structure of the subtropical circulation in the South Atlantic from three-dimensional observed velocity fields. *Deep Sea Res Part I*. <https://doi.org/10.1016/j.dsr.2014.04.015>
- Scott RB, Wang F (2005) Direct evidence of an oceanic inverse kinetic energy cascade from satellite altimetry. *J Phys Oceanogr* 35:1650–1666
- Shakespeare CJ, Arbic BK, Hogg AM (2020) The drag on the barotropic tide due to the generation of baroclinic motion. *J Phys Oceanogr* 50:3467–3481
- Shum CK et al (1997) Accuracy assessment of recent ocean tide models. *J Geophys Res* 102:25173–25194
- Smith GC, Allard R, Babin M, Bertino L, Chevallier M, Corlett GK, Crout J et al (2019) Polar ocean observations: a critical gap in the observing system and its effect on environmental predictions from hours to a season. *Front Mar Sci* 6:1025. <https://doi.org/10.3389/fmars.2019.00429>
- Souza JMAC, de Boyer Montegut C, Le Traon PY (2011) Mesoscale eddies in the South Atlantic. *Ocean Sci Discuss* 8:483–531. <https://doi.org/10.5194/osd-8-483-2011>
- Stammer D et al (2014) Accuracy assessment of global barotropic ocean tide models. *Rev Geophys* 52:243–282. <https://doi.org/10.1002/2014RG000450>
- Stammer D, Balmaseda M, Heimbach P, Kohl A, Weaver A (2016) Ocean data assimilation in support of climate applications: status and perspectives. *Ann Rev Mar Sci* 8:491–518. <https://doi.org/10.1146/annurev-marine-122414-034113>
- Storto A, Alvera-Azcárate A, Balmaseda MA, Barth A, Chevallier M, Counillon F, Domingues CM, Drevillon M, Drillet Y, Forget G, Garric G, Haines K, Hernandez F, Iovino D, Jackson LC, Lellouche J-M, Masina S, Mayer M, Oke PR, Penny SG, Peterson KA, Yang C, Zuo H (2019) Ocean reanalyses: recent advances and unsolved challenges. *Front Mar Sci* 6:418. <https://doi.org/10.3389/fmars.2019.00418>
- Taburet G, Sanchez-Roman A, Ballarotta M, Pujol M-I, Legeais J-F, Fournier F, Faugere Y, Dibarboure G (2019) DUACS DT2018: 25 years of reprocessed sea level altimetry products. *Ocean Sci* 15:1207–1224. <https://doi.org/10.5194/os-15-1207-2019>
- Tchilibou M, Gourdeau L, Morrow R, Serazin G, Djath B, Lyard F (2018) Spectral signatures of the tropical Pacific dynamics from model and altimetry: a focus on the meso-submesoscale range. *Ocean Sci* 14:1283–1301. <https://doi.org/10.5194/os-14-1283-2018>
- Tchonang B, Benkiran M, Le Traon PY, Van Gennip SJ, Lellouche JM, Ruggiero G (2021) Assessing the impact of the assimilation of SWOT observations in a global high-resolution analysis and forecasting system Part 2: results. *Front Mar Sci* 8:691–995

- Tourain C, Piras F, Ollivier A, Hauser D, Poisson JC, Boy F, Thibaut P, Hermozo L, Tison C (2021) Benefits of the adaptive algorithm for retracking altimeter nadir echoes: results from simulations and CFOSAT/SWIM observations. *IEEE Trans Geosci Remote Sens.* <https://doi.org/10.1109/TGRS.2021.3064236>
- Le Traon PY, Morrow R (2001) Ocean currents and eddies. In: L.-L. Fu and A. Cazenave (eds) *satellite altimetry and earth sciences: a handbook for techniques and applications*, pp 171–210, Academic Press, San Diego
- Le Traon, PY, G Dibarboure, G Jacobs, M Martin, E Remy, A Schiller (2017) *Use of satellite altimetry for operational oceanography in satellite altimetry over oceans and land surfaces*, CRC Press: Taylor, Editors: Stammer Cazenave. pp. 581–608. doi <https://doi.org/10.1201/9781315151779-18>
- Vergara O, Morrow R, Pujol I, Dibarboure G, Ubelmann C (2019) Revised global wave number spectra from recent altimeter observations. *J Geophys Res Oceans* 124:3523–3537. <https://doi.org/10.1029/2018JC014844>
- Verrier S, Le Traon PY, Remy E (2017) Assessing the impact of multiple altimeter missions and Argo in a global eddy-permitting data assimilation system. *Ocean Sci* 13(6):1077–1092. <https://doi.org/10.5194/os-13-1077-2017>
- Verrier S, Le Traon PY, Remy E, Lellouche JM (2018) Assessing the impact of SAR altimetry for global ocean analysis and forecasting. *J Operat Oceanogr.* <https://doi.org/10.1080/1755876X.2018.1505028>
- Vic C, Naveira Garabato A, Green JAM, Waterhouse AF, Zhao Z, Melet A, de Lavergne C, Buijsman MC, Stephenson GR (2019) Deep-ocean mixing driven by small-scale internal tides. *Nat Commun* 10:2099. <https://doi.org/10.1038/s41467-019-10149-5>
- Vivier F, Kelly KA, Thompson L (1999) Contributions of wind forcing, waves, and surface heating to sea surface height observations in the Pacific Ocean. *J Geophys Res* 104(9):20767–20788. <https://doi.org/10.1029/1999JC900096>
- Wang J, Fu LL, Torres HS, Chen S, Qiu B, Menemenlis D (2019a) On the spatial scales to be resolved by the surface water and ocean topography ka-band radar interferometer. *J Atmos Oceanic Tech* 36(1):87–99. <https://doi.org/10.1175/JTECH-D-18-0119.1>
- Wang S, Qiao F, Dai D et al (2019b) Anisotropy of the sea surface height wavenumber spectrum from altimeter observations. *Sci Rep* 9:15896. <https://doi.org/10.1038/s41598-019-52328-w>
- Waugh DW, Abraham ER (2008) Stirring in the global surface ocean. *Geophys Res Lett* 35:L20605. <https://doi.org/10.1029/2008GL035526>
- Willis JK (2010) Can in situ floats and satellite altimeters detect long-term changes in Atlantic Ocean overturning? *Geophys Res Lett* 37:L06602. <https://doi.org/10.1029/2010GL042372>
- Willis JK, Fu LL (2008) Combining altimeter and subsurface float data to estimate the time-averaged circulation in the upper ocean. *J Geophys Res Oceans* 113:C12017. <https://doi.org/10.1029/2007JC004690>
- Wunsch C (2010) Towards a midlatitude ocean frequency–wavenumber spectral density and trend determination. *J Phys Oceanogr* 40:2264–2281. <https://doi.org/10.1175/2010JPO4376.1>
- Wunsch C, Ferrari R (2018) One hundred years of the ocean general circulation. *Meteorol Monograph* 59:7.1–7.32. <https://doi.org/10.1175/AMSMONOGRAPHS-D-18-0002.1>
- Wunsch C, Gill AE (1976) Observations of equatorially trapped waves in Pacific sea level variations. *Deep Sea Res* 23:371–390. [https://doi.org/10.1016/0011-7471\(76\)90835-4](https://doi.org/10.1016/0011-7471(76)90835-4)
- Xu Y, Fu LL (2012) The effects of altimeter instrument noise on the estimation of the wavenumber spectrum of sea surface height. *J Phys Oceanogr* 42:2229–2233. <https://doi.org/10.1175/JPO-D-12-0106.1>
- Zaron ED (2017) Mapping the nonstationary internal tide with satellite altimetry. *J Geophys Res Oceans* 122:539–554. <https://doi.org/10.1002/2016JC012487>
- Zaron ED (2019) Baroclinic tidal sea level from exact-repeat mission altimetry. *J Phys Oceanogr* 49:193–210. <https://doi.org/10.1175/JPO-D-18-0127.1>
- Zhang Z, Wang W, Qiu B (2014) Oceanic mass transport by mesoscale eddies. *Science* 345:322–324
- Zhang Z, Qiu B, Klein P et al (2019) The influence of geostrophic strain on oceanic ageostrophic motion and surface chlorophyll. *Nat Commun* 10:2838. <https://doi.org/10.1038/s41467-019-10883-w>
- Zhao Z, Alford MH, Girton JB (2012) Mapping low-mode internal tides from multisatellite altimetry. *Oceanography* 25:42–51. <https://doi.org/10.5670/oceanog.2012.40>